

# Tectonics

## RESEARCH ARTICLE

10.1029/2018TC005462

### Special Section:

Fifty years of Plate Tectonics: then, now and beyond

### Key Points:

- We present a plate motion model including distributed deformation from the Triassic to the present
- The model includes most major rifts and orogens formed since the breakup of the supercontinent Pangea
- Our optimized mantle reference frame minimizes trench migration and net rotation

### Correspondence to:

R. D. Müller,  
dietmar.muller@sydney.edu.au

### Citation:

Müller, R. D., Zahirovic, S., Williams, S. E., Cannon, J., Seton, M., Bower, D. J., et al. (2019). A global plate model including lithospheric deformation along major rifts and orogens since the Triassic. *Tectonics*, 38, 1884–1907. <https://doi.org/10.1029/2018TC005462>

Received 21 DEC 2018

Accepted 23 APR 2019

Accepted article online 5 MAY 2019

Published online 17 JUN 2019

©2019. The Authors.

This is an open access article under the terms of the Creative Commons Attribution-NonCommercial-NoDeriv License, which permits use and distribution in any medium, provided the original work is properly cited, the use is non-commercial and no modifications or adaptations are made.

## A Global Plate Model Including Lithospheric Deformation Along Major Rifts and Orogens Since the Triassic

R. Dietmar Müller<sup>1</sup> , Sabin Zahirovic<sup>1</sup> , Simon E. Williams<sup>1</sup> , John Cannon<sup>1</sup> , Maria Seton<sup>1</sup> , Dan J. Bower<sup>2,3</sup> , Michael G. Tetley<sup>4</sup> , Christian Heine<sup>1,5</sup> , Eline Le Breton<sup>6</sup> , Shaofeng Liu<sup>7</sup> , Samuel H. J. Russell<sup>1</sup> , Ting Yang<sup>2,8</sup> , Jonathon Leonard<sup>1</sup>, and Michael Gurnis<sup>2</sup> 
<sup>1</sup>EarthByte Group, School of Geosciences, The University of Sydney, Sydney, New South Wales, Australia, <sup>2</sup>Seismological Laboratory, California Institute of Technology, Pasadena, CA, USA, <sup>3</sup>Now at Center for Space and Habitability, University of Bern, Bern, Switzerland, <sup>4</sup>AUGURY, Laboratoire de Géologie de Lyon, Université Claude Bernard Lyon 1, Lyon, France, <sup>5</sup>Now at Shell Global Solutions International B.V., Rijswijk, Netherlands, <sup>6</sup>Department of Earth Sciences, Freie Universität Berlin, Berlin, Germany, <sup>7</sup>State Key Laboratory of Geological Processes and Mineral Resources and School of Geosciences and Resources, China University of Geosciences, Beijing, China, <sup>8</sup>Now at Department of Earth and Space Sciences, Southern University of Science and Technology, Shenzhen, China

**Abstract** Global deep-time plate motion models have traditionally followed a classical rigid plate approach, even though plate deformation is known to be significant. Here we present a global Mesozoic–Cenozoic deforming plate motion model that captures the progressive extension of all continental margins since the initiation of rifting within Pangea at ~240 Ma. The model also includes major failed continental rifts and compressional deformation along collision zones. The outlines and timing of regional deformation episodes are reconstructed from a wealth of published regional tectonic models and associated geological and geophysical data. We reconstruct absolute plate motions in a mantle reference frame with a joint global inversion using hot spot tracks for the last 80 million years and minimizing global trench migration velocities and net lithospheric rotation. In our optimized model, net rotation is consistently below 0.2°/Myr, and trench migration scatter is substantially reduced. Distributed plate deformation reaches a Mesozoic peak of  $30 \times 10^6 \text{ km}^2$  in the Late Jurassic (~160–155 Ma), driven by a vast network of rift systems. After a mid-Cretaceous drop in deformation, it reaches a high of  $48 \times 10^6 \text{ km}^2$  in the Late Eocene (~35 Ma), driven by the progressive growth of plate collisions and the formation of new rift systems. About a third of the continental crustal area has been deformed since 240 Ma, partitioned roughly into 65% extension and 35% compression. This community plate model provides a framework for building detailed regional deforming plate networks and form a constraint for models of basin evolution and the plate-mantle system.

### 1. Introduction

Two fundamental assumptions of the plate tectonic paradigm are that tectonic plates are rigid and that they are separated by narrow boundaries (McKenzie & Parker, 1967; Morgan, 1968). The rise of space geodesy allowed Gordon and Stein (1992) to revisit these assumptions. They built a present-day deforming plate model and estimated that about 15% of Earth's surface area today is deforming along diffuse deformation zones; this was later revised to 14% (Kreemer et al., 2014). A combination of GPS, geological, and seismic observations together with a global model of rigid plate motions has been used to obtain a continuous field of present-day plate deformation (Kreemer et al., 2003, 2014). Despite the enormous advances in understanding present-day plate deformation over the past decades, to date there is no global plate model incorporating diffuse deformation for the geological past, even though a number of regional models have been published (see Gurnis et al., 2018, for a summary). This reflects that the data and computational methods needed to construct such a model through geological time are very different from present-day plate modeling approaches. The relevant geological and geophysical data are cumbersome to compile and to synthesize, and until recently, there was no community software available to build a deep-time deforming plate model. This changed recently with the release of version 2.1 of the GPlates software (Müller et al., 2018), which includes the capability to build global tectonic reconstructions with continuously evolving deforming and rigid plates

(Gurnis et al., 2018). This advance allows users to define the geometry and lifetimes of plate deformation zones between portions of the plates regarded as rigid. The deforming regions combine extension, compression, and shearing that accommodate the relative motion between rigid blocks that follow the traditional concepts of plate tectonics. Users can explore how strain rates, stretching and shortening factors, and crustal thickness evolve through space and time within deforming regions and interactively update the kinematics associated with deformation to see how these parameters are influenced by alternative scenarios (Gurnis et al., 2018). The geometries that define regions of deformation change over time in response to user-defined kinematics, and the consequences of these changes can be quantified and represented using stretching and shortening factors. Here we use these new tools to build a global deforming plate model starting with the onset of rifting within the supercontinent Pangea in the Early Triassic from ~240 Ma. This model includes deformation along most major rifts and orogens and represents a starting point for more detailed and more comprehensive future global and regional plate models with deformation.

Plate reconstructions that only consider rigid plates result in overlaps of reconstructed continental blocks in regions of subsequent extension and gaps for times succeeded by compression. Deformation has previously been implied in global plate models via such overlaps and gaps in an ad hoc fashion, without including deformation explicitly. The motivation for building a plate motion model with distributed deformation includes understanding the evolution of orogens and sedimentary basins, for example, quantifying stretching or compression factors and crustal thickness changes through time. In addition, there is a need to quantify the time dependence of continental deformation in the context of supercontinent cycles and the long-term deep carbon cycle, for example, via linking mountain building or rifting to weathering and CO<sub>2</sub> consumption or degassing (Brune et al., 2017; Godd  ris et al., 2014). Another application area for deforming plate models is a quantification of the connection between rifting, continental flooding, and sea level change (Kirschner et al., 2010). A deforming plate model also allows the restoration of the spatio-temporal relationships of data sets such as drill site locations during rifting. Lastly, a plate model including deformation provides improved surface boundary conditions for global geodynamic models with imposed plate motions (Bower et al., 2015) and may lead to an improved understanding of the connection between subduction history and distributed overriding plate deformation (Liu et al., 2017). Understanding total surface topography through time involves combining mantle convection-driven dynamic topography with isostatic topography driven by lithospheric thickness and density; this was demonstrated in a model for the evolution of the South Atlantic including South America and Africa, which combined two alternative regional deforming plate models with a mantle convection model to understand the driving forces of the evolving relief of the South Atlantic region (Flament et al., 2014).

In addition to including deformation in plate models, there is a need to improve plate-mantle reference frames in order to make these models useful for understanding the interaction of the evolving mantle through time with tectonic plates and surface topography. Previously published global plate models constructed with the aim of providing an absolute mantle reference frame either depend on particular types of geodynamic models, for example, moving hot spot models (e.g., Doubrovine et al., 2012) or may be built upon paleomagnetic data with additional imposed assumptions, such as large low-shear-velocity province fixity and empirical true polar wander corrections (Steinberger & Torsvik, 2008). Such assumptions are made to generate a mantle reference frame that is hoped to be geodynamically reasonable. However, the absolute plate motions in such models tend to result in numerous rapid changes in plate motion direction and trench migration that are disconnected from concurrent changes in mid-ocean ridge and subduction zone lengths and geometries (Matthews et al., 2016). This is problematic because the majority of the forces driving absolute plate motion originate from subduction (Conrad & Lithgow-Bertelloni, 2004) and are thought to change only when the network of plate boundaries changes substantially, particularly through collisions, including ridge-trench collisions (e.g., Yamano & Uyeda, 1985), and subduction initiation (e.g., Gurnis et al., 2004). Schellart et al. (2008) suggested that a trait of geodynamically reasonable plate models should be that trench retreat dominates over advance and that the absolute trench-orthogonal migration velocity in the central portion of long subduction zones should be small, mainly focused between rollback speeds less than 2 cm/year and trench advance speeds less than 1 cm/year. During the Cenozoic, most boundaries of rapid trench retreat are transient and limited to small plates following the initiation of subduction (Gurnis et al., 2004). Williams et al. (2015) demonstrated that most absolute plate motion models for the last 130 million years yield broad, geodynamically unreasonable distributions of slab advance and retreat

velocities. Matthews et al. (2016) found that their plate model includes several periods in which more than 20–30% of global subduction zones retreat or advance with speeds higher than 3 cm/year; this fraction reaches ~40% in the Paleozoic. Such plate model behavior is not geodynamically reasonable and results in mismatches between modeled and seismically imaged subducted slabs in global geodynamic models with imposed plate motions. Williams et al. (2015) recommended that global optimization of trench migration characteristics should be considered as a key criterion in the construction of absolute plate motion models in deep geological time. In addition, a global plate net rotation rate above 0.2–0.3°/Myr is considered geodynamically unreasonable (Becker, 2006). This condition is not well met in published plate models, for instance, the model by Matthews et al. (2016), using a hybrid reference frame of paleomagnetic data (Torsvik et al., 2012) and hot spot tracks, displays net rotation velocities (and root mean square speeds) increasing back through time far beyond reasonable limits for Early Mesozoic/Paleozoic times during which the model relies on paleomagnetic data. Rudolph and Zhong (2014) developed mantle convection models to investigate the origin of lithospheric net rotation implied by published plate motion models over the last 120–200 million years, and found that periods of high rotation in kinematic models, sometimes exceeding 0.5°/Myr, cannot be replicated by geodynamic models. In addition, high rates of lithospheric net rotation also cause mantle structure artifacts in mantle circulation models (Rudolph & Zhong, 2014). In the absence of an additional, unknown mechanism to generate the “missing net rotation,” their results imply that published absolute plate motion models contain artifacts stemming from the data and methods used to construct them. These artifacts include noisy apparent polar wander paths without longitudinal constraints, empirical true polar wander corrections, or moving hot spot models that are themselves dependent on geodynamic models, usually backward advection models, which have their own shortcomings (see Rudolph & Zhong, 2014, for a discussion). Arguably, geodynamically unreasonable fluctuations in subduction zone migration and net rotation represent absolute plate rotation noise, equivalent to the finite rotation noise found in Cenozoic relative plate motions (Iaffaldano et al., 2012). The difference is that absolute rotation noise tends to be at longer wavelengths, simply because the data constraining absolute plate motions are more widely spaced in time on average than are marine magnetic anomaly identifications. We derive an optimized mantle reference frame for our global deforming plate model to overcome these limitations, following a method developed by Tetley et al. (2019). This method minimizes both global trench motion and lithospheric net rotation, without making any explicit assumption about the relative importance of different plate driving forces.

## 2. Methods

### 2.1. Modeling Plate Deformation

The rigid global plate model we build upon is the model by Matthews et al. (2016), using the Gee and Kent (2007) timescale. In terms of relative plate motions, this model is built upon the model by Müller et al. (2016) with modifications in the western and eastern Tethys as described by Handy et al. (2010, 2015) and Zahirovic et al. (2016). The deforming plate modeling methodology followed here is described in Gurnis et al. (2018) and builds on the construction of time-dependent plate boundary mosaics called continuously closing plate models (Gurnis et al., 2012). The building blocks of a deforming plate reconstruction are points, lines, and polygons that define the boundaries between deforming and rigid regions and that can partition the deformation with the regions of deformation. Each of these geometries can be assigned its own history of motion in the same way as a plate, using Euler rotations. The spatial extent of deforming meshes is constructed based on geological and geophysical data including geological strain markers, seismic refraction profiles or published crustal thickness grids, sediment thickness for extensional regions, the topography and structure of mountain belts, and gravity and magnetic anomalies (Figure 1).

A comprehensive account of some key approaches involved in our interpretation of the oceanward limit of stretched continental crust (or boundary between continental and oceanic crust [COB]) and the landward limit of stretched continental crust (or unstretched continental crustal limit [UCCL]) from geophysical data can be found in Williams et al. (2011) and Barnett-Moore et al. (2018). Along volcanic margins, this approach includes identification of magmatic underplating, where published seismic refraction profiles are available, as for much of the North Atlantic (Barnett-Moore et al., 2018). However, such data are not available for many passive margins in more remote regions, particularly in the Indian Ocean. Further complicating factors can include the presence of transitional crust that may be either oceanic or continental or crust that may

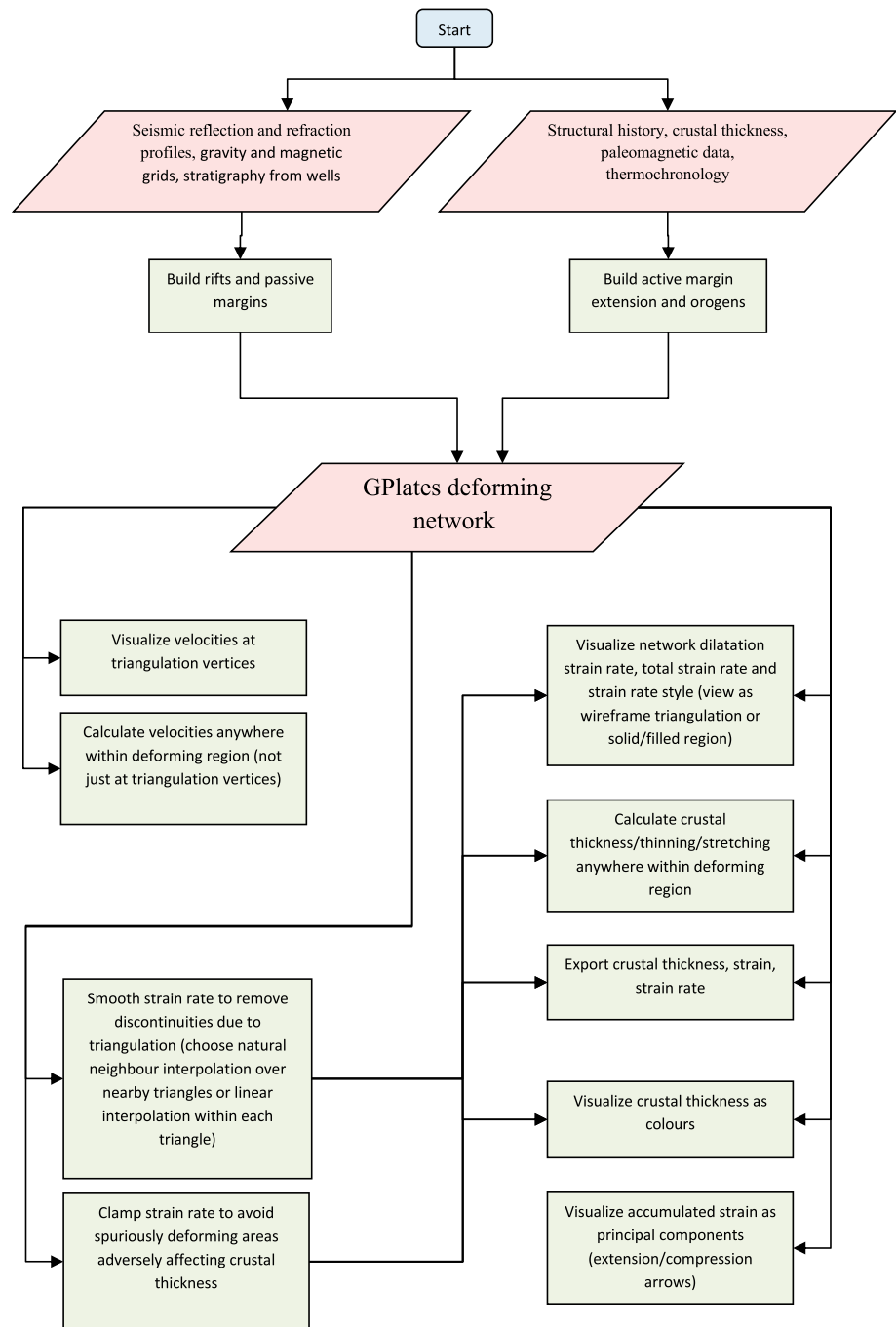


**Figure 1.** The upper part of the diagram highlights two general approaches to building a deforming region (rifts and passive margins, and active margin upper plate extension or compression) and the data typically used to define their deformation. The output of that building process is a deforming network in GPlates. The lower part of the diagram covers how a deforming network can then be further analyzed and visualized within GPlates. This includes computing instantaneous quantities of the deforming network such as velocity and strain rate, as well as the cumulative effects of the deforming network over time, including crustal thickness. Note that two boxes in the lower left feed into the four boxes in the lower right since optional modifications to the strain rate calculation (such as smoothing and clamping) also affect cumulative quantities such as crustal thickness.

correspond to exhumed continental mantle. This uncertainty can be taken into account by outlining two alternative sets of COBs, along the inner and outer boundaries of transitional crust (Barnett-Moore et al., 2018). The onset and cessation of rifting may be constrained by the stratigraphic record and tectonic

subsidence analyses, if available. In the case of passive margins, the end of extensional deformation coincides with the onset of seafloor spreading, which provides excellent constraints along most margins, unless continental breakup occurred during the Cretaceous Normal Superchron. Our method for restoring intra-continental, failed rifts follows Heine et al. (2013).

Our deforming plate workflow allows for implementing multiple rift phases if sufficient information is available to constrain their spatial extent and timing. Currently, this approach has only been implemented in the data-rich North Atlantic region (Barnett-Moore et al., 2018). Other extensional regions of our global model could easily be refined in the future in this fashion. Other issues that require special consideration include highly oblique rifting and microcontinents, that is, pieces of stretched continental crust entirely surrounded by ocean crust, formed due to ridge jumps; see Williams et al. (2011) for details how these may be included. The construction of deforming plate models for conjugate passive margins may often result in revisiting the fit and early opening history of a given margin pair to ensure that reconstructions are compliant with both geological and geophysical observations, which are complementary in the sense that geophysical data provide strong constraints for the tightness of the fit (via constraining the COB, UCCL, and crustal thickness of the rifted margin), while geological data are most useful in constraining the fit of conjugate margins along strike, for example, via matching geological features. How to build best fit models for conjugate passive margins by balancing these constraints is summarized in Williams et al. (2018).

Large regions where compressional deformation has occurred are mostly outlined by their crustal thickness anomalies, while the duration of these episodes is typically constrained by thermochronology data and reconstructed uplift or deformation histories. Building deforming plate models for other regions has included combinations of paleomagnetic data, geological strain markers from field mapping, balanced cross sections, and sometimes geodetic data (e.g., Arriagada et al., 2008; Liu et al., 2017; McQuarrie & Wernicke, 2005; van Hinsbergen et al., 2011); in addition, the relative motions of rigid plates or blocks bounding a deforming region impose additional constraints on the deformation history.

Lithospheric deformation reflects the relative motions of crustal fault-bounded blocks that extend at least through the upper crust as well as deeper deformation that is accommodated by ductile flow (Thatcher, 2009). A simplification in our approach is that we approximate plate deformation using a pure shear, uniform extension, or compression approach. This is unavoidable for kinematic plate models, as they are fundamentally incapable of capturing ductile flow. However, despite this, our approach generally works well for approximating plate deformation, at least for the crust. This is because the upper crust is brittle and elastic and faults are weaker than the adjacent crust, resulting in a block-like deformation behavior. As block size decreases, the block model approaches the deformation of a continuum, and the kinematic distinction between the two models becomes blurred (see Figure 3 in Thatcher, 2009). A good example for this is the deforming model for the Basin and Range Province in southwestern North America, implemented following McQuarrie and Wernicke (2005), composed of a large number of small rigid blocks separated by deforming regions. The deforming network for this region is also a good example for illustrating how local/regional strike-slip processes can be embedded in extending regions; see Gurnis et al. (2018) for more details.

The boundaries of deforming regions are composed of a set of intersecting lines. Each line is attached to, or moves relative to, a rigid tectonic plate. GPlates is designed to connect this set of lines, the relative position of which changes during deformation, to form closed time-dependent polygons. The relative changes in positions between lines bounding deformation zones are defined by finite rotations, analogous to the way conventional rigid plate models are built. A deforming region is called a topological network in GPlates. Its time-dependent deformation is represented by a triangulation in which the rotations and the local velocities of each node are calculated through linear interpolation within each triangle. The triangulation density in interior deforming regions (farthest from boundaries) is determined by the density of interior points placed by the user building the topologies, whereas near boundaries it is determined by the density of points along the boundary geometry.

Horizontal divergence or convergence in deforming regions results in vertically uniform thinning or thickening, and the rate of thinning/thickening is proportional to the surface dilatation rate. The surface dilatation rate (rate of change of surface area per unit area) is calculated from the divergence of the surface velocity field in the deforming region, as follows:  $DH/dt = -H * \text{dilatation\_rate} = -H * \text{divergence (velocity)}$ , where  $H$  is thickness. Each triangle in the deforming mesh has a velocity gradient calculated from its three



vertex velocities, and smoothing can optionally be applied to these gradients. The stretching/compression ( $\beta$ ) factor is  $\beta = H_i/H$ . Here  $H_i$  is initial crustal thickness, and  $H$  is determined by integrating  $DH/dt = -H \cdot \text{divergence (velocity)}$  over time. Values greater than 1 represent extensional regions, and values between 0 and 1 represent compressional regions. The thinning/thickening ( $\gamma$ ) factor is  $\gamma = (1 - H/H_i)$ . Here values between 0 and 1 represent extensional regions, and negative values represent compressional regions. Synrift subsidence in extending regions is linearly related to  $\gamma$ , as is uplift in compressional regions. In addition to computing and visualizing  $\beta$  and  $\gamma$  factors in deforming regions, crustal (or plate) thickness can be computed and displayed in GPlates by specifying a given initial crustal (or plate) thickness (Figure 1).

A simplification in our current model is the absence of deformation partitioning within rift zones; that is, there is currently no distinction between high extension factors expected in central rift areas and the more moderate amounts of extension closer to the rift edge; instead, the displayed values represent average stretching factors for each margin segment that vary along strike. The reconstruction here is limited to the time between 240 Ma and present day. While this time period captures the majority of rifting that has shaped Pangea's margins, there are continental margins whose extension started during the Paleozoic (e.g., the Northwest Shelf of Australia). Considering these earlier extension phases is beyond the scope of this paper. Equally, our model does not include a number of intracontinental rifts or the complex Jurassic–Cretaceous deformation history of western North America (Sigloch & Mihalynuk, 2017), much of which is not well enough constrained in space and time to be implemented in our current model. In the case of orogenesis, the crustal thickness evolution implied by our approach is generally an overestimation as it does not account for the inevitable erosion that would accompany uplift. However, future links to surface process models will address the lack of erosion and deposition that would occur as a result of compression or extension of lithosphere.

We assimilate observations constraining plate deformation into a model of rigid plate motions and compute time-dependent uniform stretching, compression, and strain rates within deforming regions based on the kinematic motions of the rigid surrounding blocks. The technical details of implementing plate deformation can be found in Gurnis et al. (2018) and in GPlates software tutorials (<https://sites.google.com/site/gplates-tutorials/>). To infer stretching factors, an estimate of the crustal thickness prior to extension must be made, usually based on seismological crustal thickness measurements from unstretched regions along a given zone of extension.

## 2.2. Absolute Plate Model Optimization

We apply a recently developed approach to reconstructing absolute plate motions in a mantle reference frame using a joint global inversion of multiple constraints including hot spot location and associated trail data for the last 80 million years, global trench migration behavior, and estimates of net lithospheric rotation (Tetley et al., 2019). The unoptimized model is our global deforming plate model with a hybrid reference frame corresponding to that used in Matthews et al. (2016). Prior to the main iterative optimization stage of the workflow, some initial data preprocessing stages are carried out. First, subduction zones are reconstructed in 10-million-year intervals and stored in files ready for quick retrieval during the optimization. This is done as a preprocessing step as resolving the boundaries of continuously closing plates and deforming networks is time consuming. Next, age-coded hot spot trails are interpolated at 5-million-year intervals for 80 Ma to the present. Subsequently, net rotations are computed and exported using GPlates to generate a time sequence of total net rotations from the starting rotation model. These are used in turn to create a no-net-rotation model used in the optimization stage. In the optimization stage the large total number of candidate global plate models is associated with a computational cost that is proportional to the number of plate IDs in the rotation files, so performance is dramatically improved by reducing the set of rotations in an additional preprocessing stage to only those plate circuit paths supporting the plate IDs required by the optimization process.

The aim of the optimization is to find absolute plate rotations for Africa that minimize global net rotation and global trench migration velocities, with a user-provided weighting, while fitting both the geometry and age progression of age-dated hot spot tracks. Here we restrict ourselves to using eight well-studied present-day hot spot locations including the Cobb, Foundation, St. Helena, Tristan, Réunion, Tasmanid, Samoa, Louisville, and Hawaii hot spots and their associated hot spot trails and age dates (Tetley et al., 2019). The optimization approach involves generating optimized Africa rotations from 0 to 240 Ma in 10-

million-year intervals progressing backward in time. To find the globally optimized rotation in 10-million-year intervals, a random distribution of 100 starting rotation poles is projected onto the sphere within a circle with a radius of  $60^\circ$  centered on a starting stage rotation pole of Africa relative to the spin axis calculated from global paleomagnetic data (Torsvik et al., 2012) with a quality score of  $Q \geq 3$ , using Van der Voo (1990) quality criteria. Each of those random starting rotations is then minimized within its local neighborhood by iteratively perturbing the pole latitude, longitude, and angle of the starting rotation, evaluating a cost equal to the sum of individual constraints (involving global net rotation, trench migration, and hot spots) and converging to the locally perturbed rotation with the minimum cost. See Tetley et al. (2019) for additional details. Since the local minimizations are independent of each other, they are distributed over multiple cores in a high-performance computing cluster using mpi4py (Python bindings for Message Passing Interface).

The net rotation constraint cost is based on computing the global net rotation  $\omega_{\text{net}}$  calculated as implemented in GPlates (Müller et al., 2018), following Torsvik et al. (2010). It is computed via an offset of the Africa rotation in the perturbed rotation model compared to the no-net-rotation model. The constraint cost for trench migration is the mean of the trench-normal velocity vector, resulting from the perturbed rotation model, plus the standard deviation in order to converge on models that minimize global trench-normal velocities (and velocity variations). The total cost  $J$  is therefore calculated as follows:

$$J = \frac{HS_m}{\sigma_1} + \frac{TM_k}{\sigma_2} + \frac{\omega_{\text{net}}}{\sigma_3} \quad (1)$$

where  $HS_m$  is the global hot spot trail misfit,  $TM_k$  is the global trench migration kinematics value, and  $\omega_{\text{net}}$  is the calculated rate of net lithospheric rotation, while  $\sigma_1$ ,  $\sigma_2$ , and  $\sigma_3$  are the relative weightings for each constraint, with hot spot trail misfits only used for the last 80 million years.

The constraint cost for hot spots is the median trail misfit distance (between observed trail and trail predicted by the perturbed rotation model) plus the standard deviation. In this approach the motion of individual hot spots relative to the Earth's spin axis through time is obtained through the optimization process rather than via a mantle convection model (Tetley et al., 2019). A relative weighting can be applied to each constraint before summing for a total cost. In our case the hot spot constraint is only included for times between 0 and 80 Ma, and the net rotation constraint has half the weight for 80–240 Ma. We prefer to assign a smaller weight to net rotation because the need to construct synthetic oceanic plates to generate complete global plate models for the geological past contaminates net rotation results in ways that are difficult to quantify. A parameter sensitivity analysis, including a comparison of the results with a diverse suite of absolute plate motion models, can be found in Tetley et al. (2019).

### 2.3. Revised Oceanic Age Grids

Our deforming plate model is accompanied by a set of grids of the paleo-age of the ocean floor in 1-million-year intervals. The grids are updated with respect to the grids by Müller et al. (2016) in a number of ways, incorporating revisions of the regional plate tectonic evolution as described in the next section. Major changes have been made in the eastern Tethys following Zahirovic et al. (2016), with minor updates in the Arctic, the Mediterranean, and the Caribbean/equatorial Atlantic. The age gridding is now carried out using spherical interpolation (Wessel et al., 2013), resulting in a major improvement, particularly for the Arctic region.

## 3. Deforming Regions Within the Global Plate Model

### 3.1. North Atlantic Region

The oldest deforming network in our model represents rifting between Africa and North America, which we implement following Kneller et al. (2012) in terms of its geometry and its Early Triassic initiation age of 240 Ma and a rift cessation age of 155 Ma, leading to the opening of the central North Atlantic. Our model for the progressive rifting of the remainder of the North Atlantic is based on Barnett-Moore et al. (2018). In this model rifting between Greenland and northern Europe is active from 200 to 120 Ma (Figure 2); at this time the rift geometry north of the Iberian-Newfoundland conjugate margins changes to reflect rifting between Greenland and North America from 120 to 61 Ma, while rifting between Greenland and northern Europe ceases temporarily until starting again at 79 Ma, leading to a second phase of rifting in this region, which

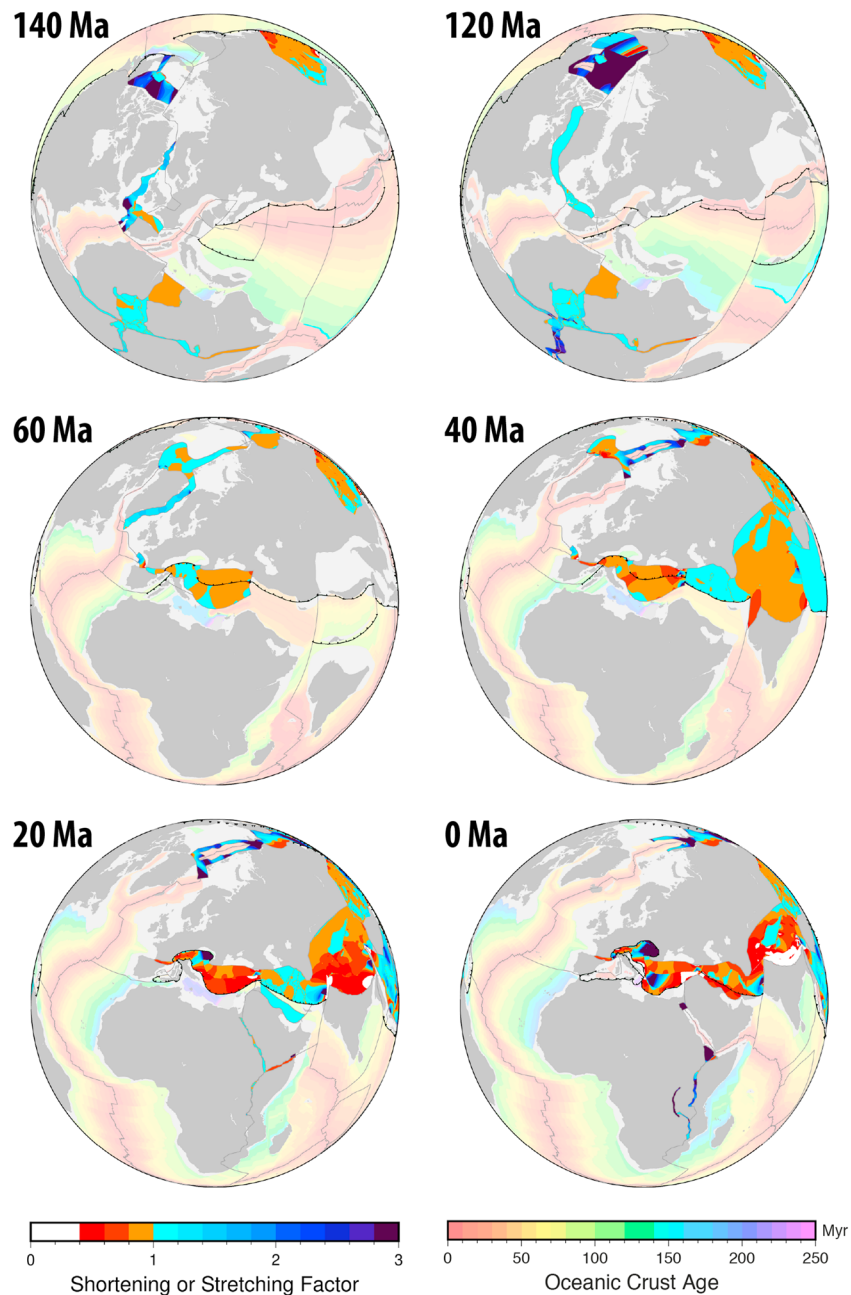


**Figure 2.** Cretaceous and Cenozoic plate deformation around the Arctic, eastern Asia, and North America. Continents are shown in medium gray, with submerged continental regions (relative to present-day coastlines) in light gray. The paleo-age of the ocean crust is outlined in light colors progressing from red to green, blue and magenta from young to old crust. Subduction zones are black lines with triangles, while mid-ocean ridges are shown as light gray lines. Deforming regions are outlined in light to dark blue colors if in extension, denoted by a stretching factor  $>1$ , while plate compression is outlined in orange/red colors, denoted by a compression factor  $<1$ . Orthographic projection.

lasts until about 56 Ma when breakup occurs (Barnett-Moore et al., 2018). Deformation between Iberia and the remainder of northern Europe lasts until 34 Ma (Barnett-Moore et al., 2018), marking the end of major continental deformation related to the opening of the Atlantic.

### 3.2. Arctic Region

The Arctic region has experienced numerous periods of deformation starting in our model with Early Jurassic (~195 Ma) rifting between the North Slope of Alaska and the northern Canadian margin (Embry



& Dixon, 1990). Our deforming model follows the rigid plate model by Shephard et al. (2013), using crustal thickness models (Pease et al., 2014; Petrov et al., 2016) to delineate the spatial extent of deforming regions. The extent of the Canada and Amerasia ocean basins has been updated based on the crustal structure of Petrov et al. (2016), significantly reducing the extent of oceanic crust compared to our previous rigid plate model (Müller et al., 2016). We model the initiation of seafloor spreading in the Canada and Amerasia basins at 145 and 160 Ma, respectively, following Shephard et al. (2013) (Figure 2).

We model the crust that underlies the Aleutian Basin as a trapped piece of 83- to 68-million-year-old Pacific Ocean crust (Scholl et al., 1975) with entrapment occurring at 46 Ma. A recent crustal velocity structure analysis of the Aleutian Basin failed to find differences in crustal structure to support an alternative back-arc basin model (Christeson & Barth, 2015). The opening of the Makarov Basin between the Alpha and Lomonosov Ridges from 57 to 69 Ma is modeled after Alvey et al. (2008) and Døssing et al. (2017) (Figure 2). The counterclockwise rotation of Greenland relative to North America in the course of the opening of the Labrador Sea and Baffin Bay resulted in the Eurekan Orogeny from 68 to 19 Ma, implemented following Gion et al. (2017).

### 3.3. South Atlantic Region

In most global plate kinematic models, the African plate occupies a position in the top of the rotation tree hierarchy with post-Jurassic plate motions relative to it, specified through in situ ocean basin records. Hence, constructing the internal Mesozoic deformation history of Africa and its conjugate passive margin systems is a critical step toward more precise global plate kinematic models. Our deforming plate model for the South Atlantic Rift system, encompassing Africa and South America, is built on the rigid plate model by Heine et al. (2013) and starts with intracontinental deformation in the Patagonian part of South America at 150 Ma (Figure 3). Here Jurassic-aged basins in between rigid continental blocks define a broad area of lithosphere extension between Antarctica, southern Africa, and South America predating the formation of the main South Atlantic rift (Heine et al., 2013; König & Jokat, 2006; Macdonald et al., 2003). From 145 Ma the main South Atlantic and intraplate African rifts document the formation of a Gondwana-wide network of transient, divergent plate boundaries (Chang et al., 1992; Genik, 1992; Heine et al., 2013), marking the final phase of supercontinent dispersal. Using the rift basin architecture to derive quantitative estimates of extension directions and amount of extension, the plate kinematic models provide a quantitative framework for the pre-breakup kinematics of the South Atlantic rift. Rift obliquity causes the termination of extension in unfavorably oriented rift branches in Africa and South America around the early Aptian, leading to diachronous continental breakup between South America and Africa and the formation of the equatorial Atlantic oceanic gateway around 105 Ma (Heine & Brune, 2014; Heine & Müller, 2005). The model also includes compressive deformation along the Patagonian Andes from 150 to 126 Ma (Flament et al., 2014) and from 45 Ma to the present day along the central Andes based on Arriagada et al. (2008). Miocene compression along the northern Andes after 20 Ma is based on Pindell and Kennan (2009). The geometry of the deformation associated with the opening of the Scotia Sea, postdating 50 Ma, follows Eagles and Jokat (2014) and Nerlich et al. (2013) and persists to the present.

#### 3.3.1. African Region

This section is focused on the Cenozoic East African rift, as our implementation of Cretaceous rifts in Africa are found in the South Atlantic section. We implement the East African Rift following the rigid plate model of Iaffaldano et al. (2014), with motion between Somalia and Southern Africa initiating from 19.7 Ma. The geometry of the rift system is based on Chorowicz (2005). The incorporation of an independent Somalia Plate results in a plate hierarchy for Central Indian Basin motion relative to the South Mascarene Basin between 55.9 and 40.1 Ma (magnetic chrons 25y and 18, respectively), rather than moving relative to Southern Africa, as in our previous rigid plate model (Müller et al., 2016).

### 3.4. North America, Gulf of Mexico, and Caribbean Regions

The model for the circum-Caribbean region is largely based on the rigid plate model by Müller et al. (2016), which is primarily based on Boschman et al. (2014) with some modifications. We have extended the central North Atlantic spreading ridge southward to the west of the Demerara Rise from 175 Ma, forming a small pocket of Jurassic-aged oceanic crust offshore Guyana bounded by the Demerara-Guinea transform to the north (Reuber et al., 2016). Spreading along this segment continued until the inception of the Equatorial Atlantic spreading system at 120 Ma. Rifting between North and South America is contemporaneous with

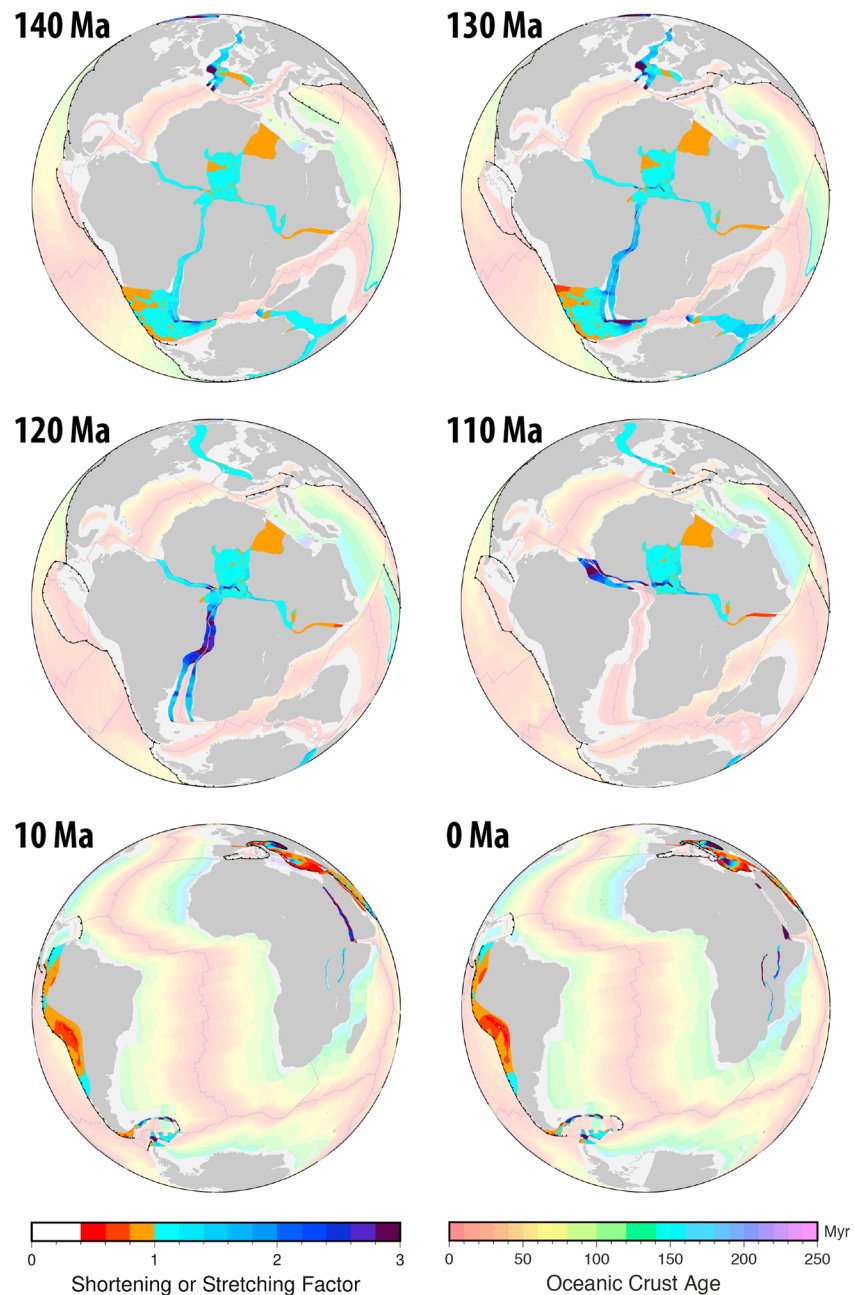


**Figure 3.** Cretaceous to present plate deformation in the Atlantic Ocean. See Figure 2 caption for details.

the onset of rifting between North America and Africa at 240 Ma, persisting until about 150 Ma when seafloor spreading along the proto-Caribbean gateway commenced (Müller et al., 2016; Figure 3). Late Triassic to Middle Jurassic divergence between North America and the Yucatan block led to continental rifting along the future Gulf of Mexico (Marton & Buffler, 1994) starting around 190 Ma, translating the Yucatan and Florida-Bahamas blocks southeastward relative to North America. Subsequently, from 170 to 158 Ma, the Yucatan block is separated from southern Florida terranes by a complex NW trending Jurassic rift system leading to a separation of the Yucatan block from southern Florida terranes and extension of the Florida-Bahamas block (Marton & Buffler, 1994). The following phase of Early Cretaceous proto-Caribbean seafloor spreading between the Americas is accompanied by a Cretaceous Quebradagrande back-arc basin along the northern Andean margin from 145 to 100 Ma (Braz et al., 2018), which is included in our model (Figure 3). Basin and Range Province extension since 36 Ma is based on McQuarrie and Wernicke

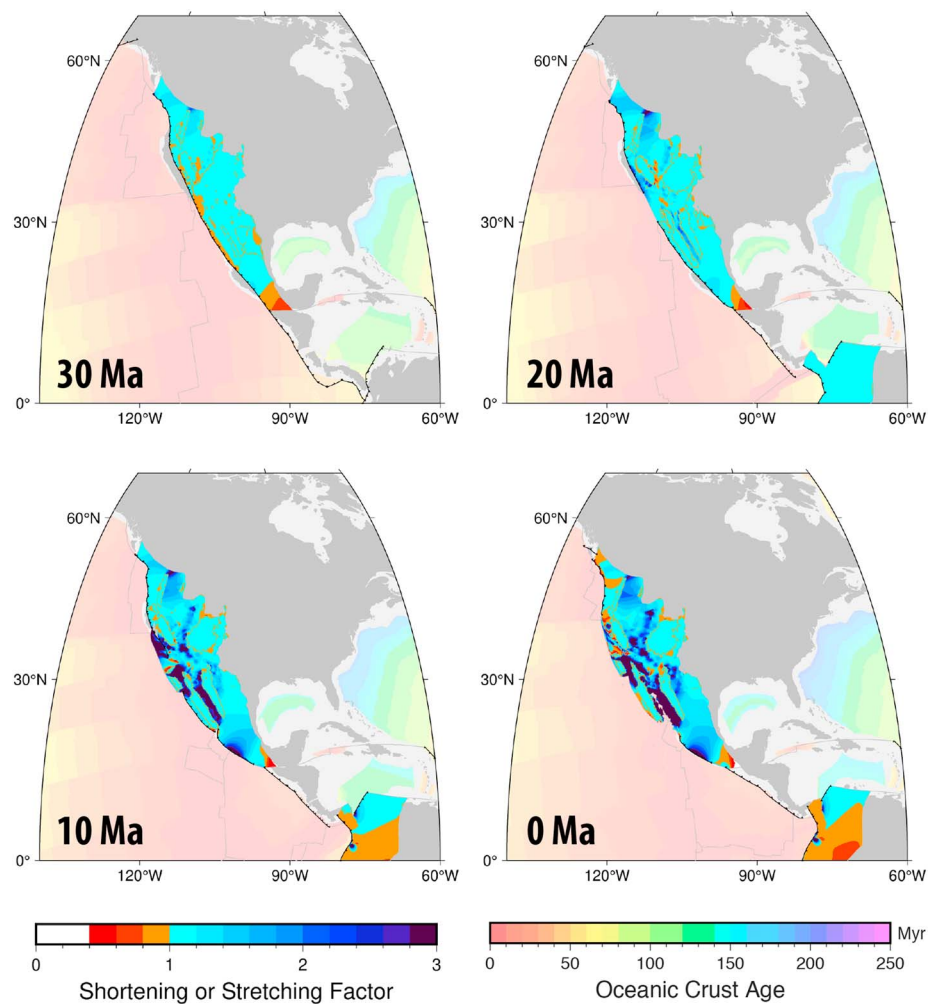


**Figure 4.** Neogene deformation in western North America. See Figure 2 caption for details.

(2005) (Figure 4). The implementation of this model is described in detail in Gurnis et al. (2018). Extension around the Gulf of California, initiating at 12 Ma, follows Stock and Hodges (1989), with the onset of seafloor spreading in the southern Gulf of California at ~3.5 Ma (Figure 3). The spatial extent of the deforming mesh is based on the regional crustal thickness map from Lewis et al. (2001).

### 3.5. Indian Ocean Region

Contemporaneous with Jurassic rifting in the North Atlantic, rifting between Africa, East Antarctica, and India initiates around 180 Ma and ceases with the onset of seafloor spreading around 148 Ma, while rifting between India, West Australia, and Antarctica is active from about 160 to 126 Ma (Figure 5); see Gibbons et al. (2013) for a summary of constraints. Most of the passive margin extension of northern Greater India, as reflected in Tethys Himalaya sections, is Paleozoic and thus predates our current model (Sciunnach & Garzanti, 2012). However, regional sedimentary sections suggest some minor Jurassic rifting (Sciunnach & Garzanti, 2012). Jurassic rifting is also well documented along the northern margin of Papua New Guinea. Here we follow the model by Gibbons et al. (2015) to include a short-lived rifting event along northern Greater India in the Late Jurassic. Rifting between Australia and East Antarctica initiates at 160 Ma and ends at ~83 Ma, following the models by Williams et al. (2011) and Kharazizadeh et al. (2016) to constrain the timings and regional geometry through time of this rift system (Figure 5). Many alternative models for the rifting and breakup history of this region have been published, putting emphasis on interpretations of different sets of regional geological or geophysical data. These models are evaluated in Williams et al. (2018), illustrating why a balanced combination of geological and geophysical observations does not lead to reconstructions such as that by White et al. (2013), which features an extant ocean basin between

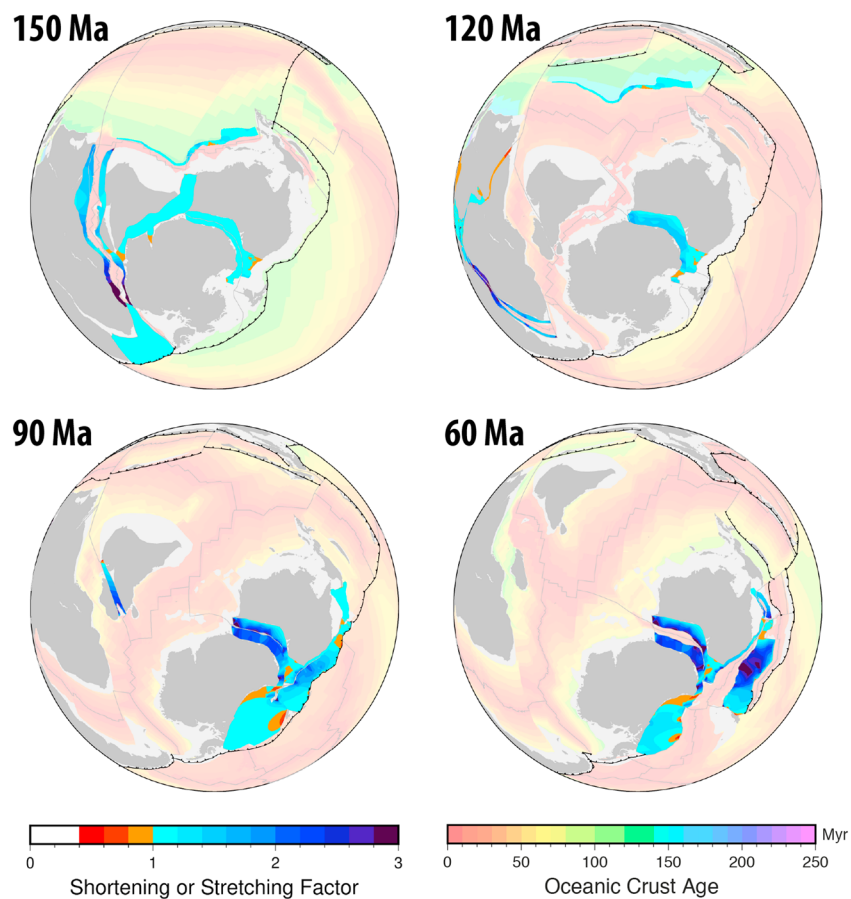


**Figure 5.** Jurassic to Eocene breakup of Gondwana and plate deformation in the Indian Ocean, Zealandia, and West Antarctica. See Figure 2 caption for details.

Australia and East Antarctica for much of the Mesozoic, for which there is no evidence. The central Indian Ocean plate deformation zone (Kreemer et al., 2003) is not included in our model as we are focused on deforming continental crust.

### 3.6. Tethys Ocean and Southern and Eastern Eurasian Margins

The Mesozoic and Cenozoic geological evolution of the Tethys eastward to Southeast Asia has been dominated by convergent tectonics, with major episodes of orogenic growth as part of the Africa-Eurasia, India-Eurasia, and Australia-Asia collision systems. However, major extension occurred contemporaneously in adjacent regions, leading to a complex deformation history. The earliest collision occurred along the Alpine chain in the Dinarides, starting around 67 Ma and recording a complex series of events driven by Adria-Europe collision and subduction zone dynamics including switches in subduction polarity and slab tearing (Handy et al., 2015; Figure 2). Our reconstruction of the region is based on the rigid plate model of Hosseinpour et al. (2016) with modifications following published tectonic reconstructions of the western Mediterranean area (van Hinsbergen et al., 2014), the Adriatic plate (Le Breton et al., 2017), the so-called AlCaPa (Alps-Carpathians-Pannonian) and the Tisza and Dacia continental blocks involved in the Alpine orogen (Handy et al., 2010, 2015). The timing and outlines of deforming regions since 67 Ma broadly follow Handy et al. (2015) (Figure 2). We have implemented an early to middle Carboniferous age ( $340 \pm 25$  Ma) for the Herodotus Basin within the eastern Mediterranean based on Granot (2016).

The deforming model for the central and eastern Tethys and adjacent regions in Eurasia is embedded in the rigid plate reconstructions of Zahirovic et al. (2016), where the India-Eurasia continent-continent collision initiates at  $\sim 45$  Ma and boundaries of deforming regions are delineated using a combination of crustal thickness and gravity anomaly data (Figure 6). The extent of Greater India is taken from Gibbons et al. (2015), and



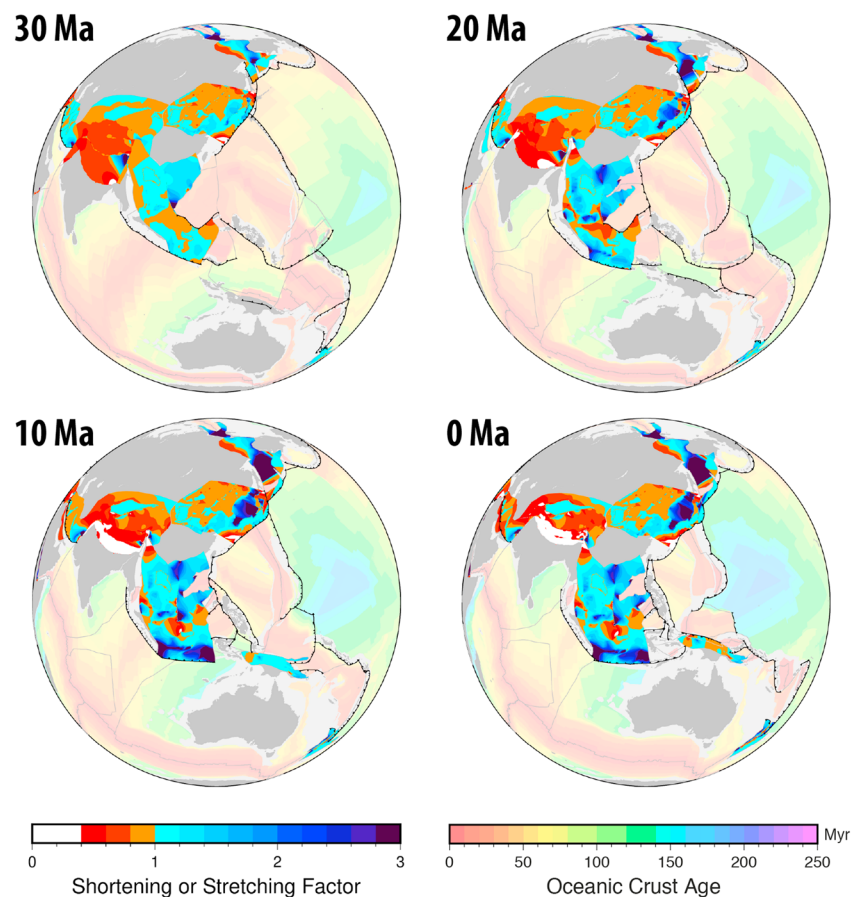


**Figure 6.** Cenozoic plate deformation in Asia and Zealandia. See Figure 2 caption for details.

the deforming Eurasian margin is implemented largely following the regional deformation synthesis of van Hinsbergen et al. (2011). However, the precollisional position of Lhasa in our model is further south at  $\sim 15^\circ\text{N}$  than it is in van Hinsbergen et al. (2011), largely based on the 53-Ma paleomagnetic-derived latitude of  $14.4^\circ\text{N} \pm 5.8^\circ\text{N}$  for mafic dykes intruding the Linzizong Formation (Liebke et al., 2010).

The collision between Arabia and Eurasia is initiated at 40 Ma and implemented following the model by McQuarrie and van Hinsbergen (2013) for the Zagros region. The oroclinal bending of Sundaland resulting from the India-Eurasia collision to the west and the Australia-Asia collision to the east captures the broad deformation style of this region as represented in the model of Yang et al. (2016). How this model was constrained and implemented is described in Gurnis et al. (2018). Deformation associated with the opening of the South China Sea since 40 Ma follows the model by Bai et al. (2015), including the delineation of boundaries of deforming regions (Figure 6). The model for Mesozoic–Cenozoic deformation of Northeast Asia is taken from Liu et al. (2017). Deformation starts with NW-SE oriented shortening from 200 to 137 Ma, followed by several phases of extension and compression with varying orientations, culminating in roughly N-S oriented extension in the Cenozoic (Liu et al., 2017; Figure 2).

### 3.7. Australasia, Zealandia, and Antarctica

Australasia is a region characterized by complex deformation, mainly reflecting the effects of adjacent plate collisions. The onset of rifting between Australia's eastern margin and Zealandia is constrained to have commenced around the mid-Cretaceous ( $\sim 100$  Ma) based on the widespread occurrence of felsic volcanism in New Zealand and the Lord Howe Rise, thought to be linked to crustal thinning (Tulloch et al., 2009). The magnitude of extension in this region in our model is based on the crustal thickness model by Grobys et al. (2008). Rifting east of Australia ceased with the onset of seafloor spreading in the Tasman Sea, starting around 80 Ma in the southern Tasman Sea and at 58 Ma in the northernmost Tasman Sea (Müller et al.,



2016). Rifting in the Coral Sea between 90 and 52 Ma is implemented following the crustal thickness model of Segev et al. (2012) and the rigid plate model of Müller et al. (2016). Along Papua New Guinea's northern margin, compression initiated around 15–14 Ma, driven by the Halmahera Arc colliding with New Guinea, along the New Guinea Mobile Belt (Figure 6; Baldwin et al., 2012; Zahirovic et al., 2016). Cenozoic deformation within Zealandia postdating 40 Ma is implemented following the rigid plate model by Wood and Stagpoole (2007). The West Antarctic Rift system was initiated in the mid-Cretaceous and can be separated into a Cretaceous rift event between 105 and 90 Ma (Figure 5) contemporaneous with the separation between West Antarctica and southern Zealandia (Wobbe et al., 2012) and an Early Cenozoic rift stage starting in the Eocene with continuous slow extension between these two events (Matthews et al., 2015). The outline of the rift in our model follows Wilson and Luyendyk (2009).

## 4. Results and Discussion

### 4.1. Evolution of Plate Deformation

Our global deforming plate model has been integrated with an updated set of paleo-age grids of the ocean crust through time (Figures 7a and 7b). These grids are constructed following the method described in Müller et al. (2016). At present day, our model includes an area of about 8% of the Earth's surface where distributed deforming of the lithosphere occurs. This value is significantly smaller than Kreemer et al.'s (2014) estimate of 14%. The reason for the discrepancy is that we solely focus on deformation of continental lithosphere. Therefore, our model excludes large deforming regions in ocean basins, particularly in the Indian Ocean. Our model also excludes deforming edges of overriding plates along subduction zones, which form another significant portion of Kreemer et al.'s (2014) geodetic strain-rate model. Here we review the evolution of lithospheric stretching and shortening since 240 Ma.

In the Jurassic, distributed plate deformation reaches a maximum around ~160–155 Ma, covering  $\sim 30 \times 10^6$  km<sup>2</sup>, largely driven by a vast network of extending continental margins, dropping to a third of this size in the mid-Cretaceous (~105 Ma; Figure 8). Distributed extension decreases throughout the Late Jurassic to the Early Cretaceous (155–110 Ma; Figure 8), reflecting the onset of seafloor spreading along many rift systems (Figure 7). The continental area subject to compression increases roughly in parallel with increasing rift area after 200 Ma, fluctuating between  $4$  and  $7 \times 10^6$  km<sup>2</sup> between 190 and 70 Ma. Starting at 70 Ma, and accelerating after 50 Ma, the continental area in compression rises to a peak of  $\sim 25 \times 10^6$  km<sup>2</sup> at 35 Ma (Figure 8), initially reflecting the Late Cretaceous onset of the Alpine collision along southern Europe, and after 50 Ma the onset of the India-Eurasia collision, followed by other collisions along Eurasia's margins (Figure 7). After 100 Ma, the total extensional area increases due to the extension within Zealandia and a partial switch from compression to extension in Northeast Asia (Figure 7). The total area of plate deformation reaches a high of  $\sim 50 \times 10^6$  km<sup>2</sup> in the Early Miocene (~20 Ma) mainly driven by the progressive growth of plate collisions in the Cenozoic.

The vast proportion of all plate areas in extension are stretched in the range of beta (stretching) factors of 1–2 (Figure 8). A peak in more highly extended regions (beta = 2–3) occurs at 155 Ma ( $\sim 4 \times 10^6$  km<sup>2</sup>), reflecting the peak of extension during the Jurassic breakup of Pangea (Figure 8). In the Late Cretaceous (~90–60 Ma) and Late Cenozoic (~20–0 Ma) broad peaks of the area stretched by factors larger than 2 occur, reflecting the formation of highly extended regions in Southeast and Northeast Asia, within Zealandia and between Australia and Antarctica (Figure 7). Extension by factors larger than 3 is rare, never amounting to more than a maximum of about  $1 \times 10^6$  km<sup>2</sup> (Figure 8). Cumulatively, 35% of the total area of continental crust has been deformed. About two thirds of the area subject to deformation over the last 240 million years has been extended, while one third has been compressed (Figure 8). Before the disintegration of the supercontinent Pangea started at 240 Ma, we estimate the continental area to have been about  $198 \times 10^6$  km<sup>2</sup>. The combined action of extension and compression has resulted in a net increase of the area to about  $220 \times 10^6$  km<sup>2</sup> at present day, that is, roughly a 10% increase in area. We may speculate that by the time the next supercontinent has formed, this net gain in area will be much reduced or even reversed by the progression of future plate collisions. As we are unable to investigate plate deformation over a full supercontinent cycle, it remains unknown what the continental crustal area evolution from one supercontinental assembly to the next may be. In addition, our model does not take into account continental crustal growth by accretionary processes or loss via tectonic erosion along subduction zones.

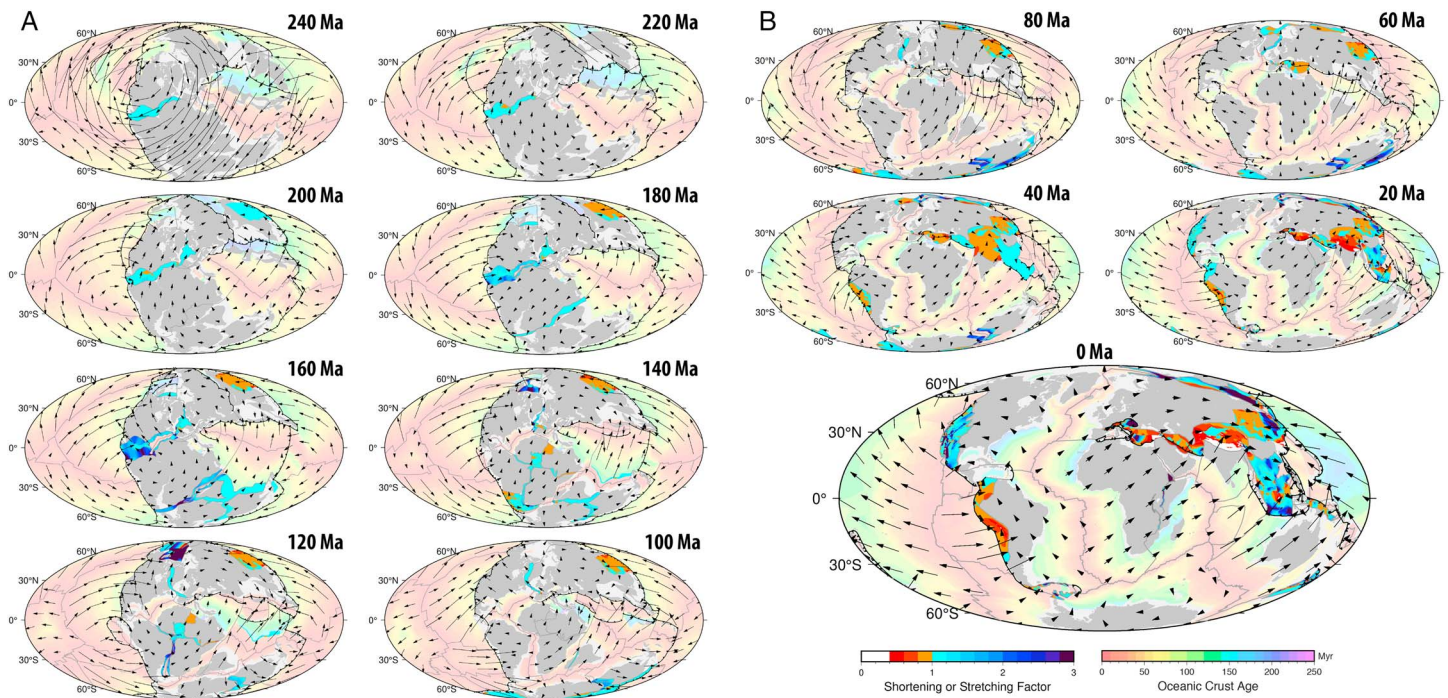


**Figure 7.** Plate reconstructions for the Triassic to present, showing continents in medium gray, with submerged continental regions (relative to present-day coast-lines) in light gray. The paleo-age of the ocean crust is outlined in light colors progressing from red to green, blue and magenta from young to old crust. Subduction zones are black lines with triangles, while mid-ocean ridges are shown as light gray lines. Deforming regions are outlined in light to dark blue colors if in extension, denoted by a stretching factor  $>1$ , while plate shortening is outlined in orange/red colors denoted by a shortening factor  $<1$ . Absolute plate velocities in a mantle reference frame are shown as black arrows. Hammer projection.

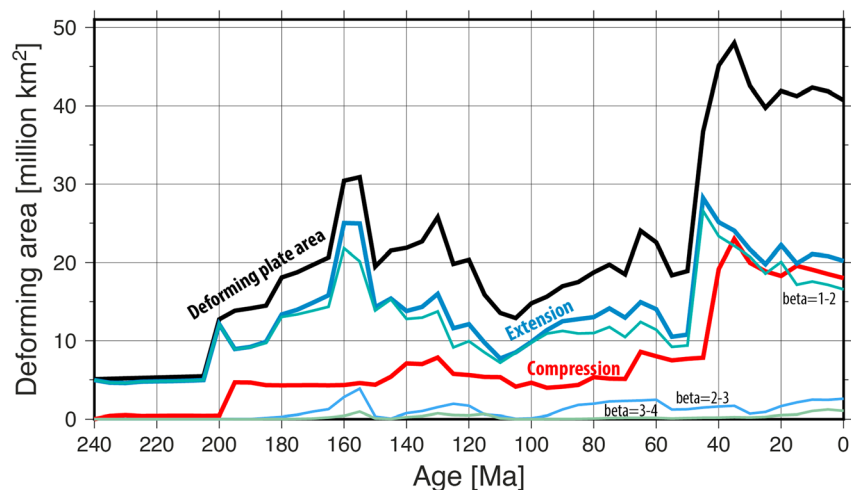


**Figure 8.** Total deforming plate area through time (black) from the Early Triassic to present, separated into areas of shortening (red) and areas in extension (blue). Extensional regions are further separated into those with stretching factor  $\beta = 1-2$  (turquoise),  $\beta = 2-3$  (light blue), and  $\beta = 3-4$  (light green). Note the peak in total extensional areas at 160–155 Ma, reflecting the vast extension of Pangea's rift system in the Late Jurassic, and the rise in compression after 50 Ma, mainly representing the progressive growth in collisions along southern Eurasia. The increasing length of rift systems after 50 Ma (see Şengör & Natal'in, 2001), mainly reflecting extension in Asia, is partly driven by the India-Eurasia collision and partly by interactions between subducting slabs and overriding plates along the western and eastern Pacific rim.

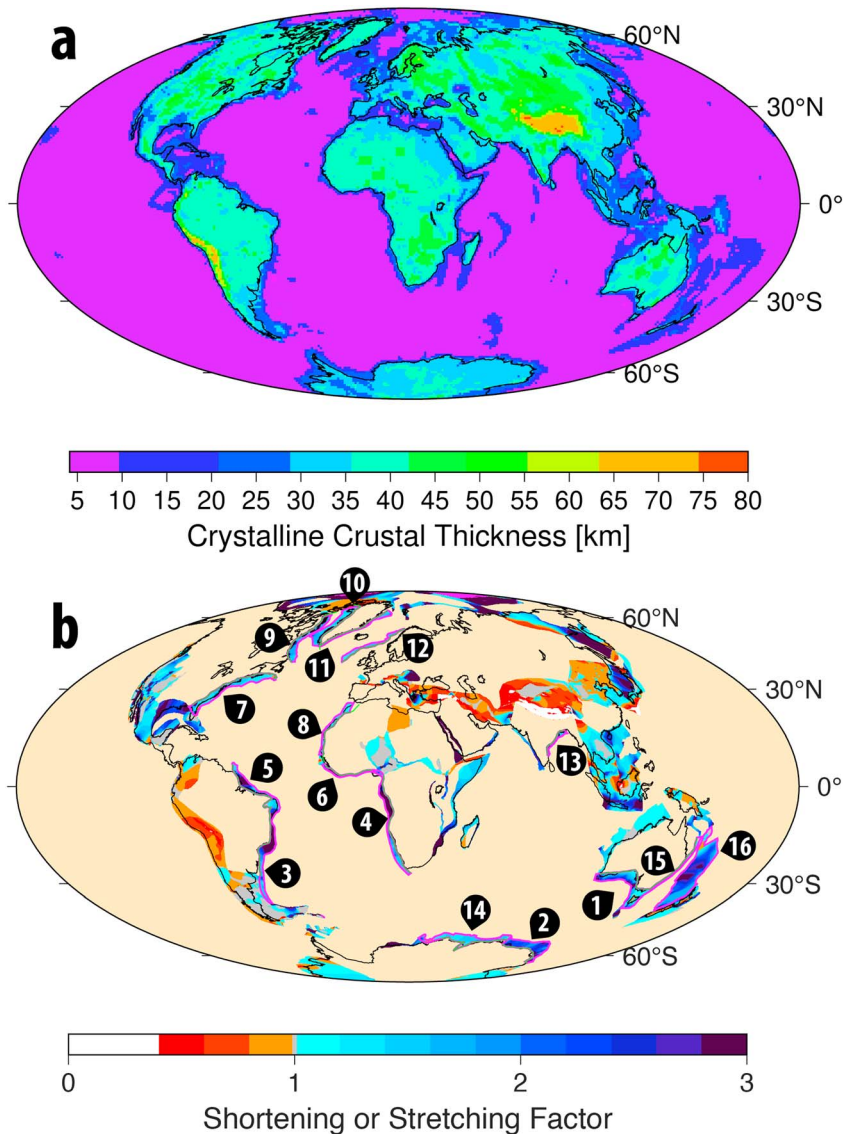


**Figure 9.** (a) Crystalline crustal thickness with histogram-equalized color scale from CRUST 1.0 (Pasyanos et al., 2014). (b) Total distributed continental deformation accumulated over 240 million years of rifting and compression. The total area covered by continental crust is  $219.7 \times 10^6 \text{ km}^2$  (43% of the total surface area), while the area covered by ocean crust is  $290.4 \times 10^6 \text{ km}^2$ . A total of about 35% of the continental crustal area has been deformed over the last 240 million years, partitioned into  $\sim 50.5 \times 10^6 \text{ km}^2$  that have been extended ( $\sim 65\%$ ) and  $\sim 27 \times 10^6 \text{ km}^2$  that have been compressed ( $\sim 35\%$ ). This is a minimum estimate. Some key passive margins are numbered, and crustal thicknesses are analyzed in Figure 10.

#### 4.2. Model Uncertainty

Our deforming plate model can be used to compute a variety of quantities, including the evolution of finite strain, crustal thickness, lithospheric temperature, isostatic topography, and heat flux (Gurnis et al., 2018), helping with validating the model if appropriate observations are available. For extending regions, the uncertainty of a deforming plate model can be estimated by comparison of observed versus predicted crustal thickness or stretching factor estimates from stratigraphic successions derived from exploration wells with modeled stretching factors; for compressional regions, this approach is more difficult because thickened crust is not preserved due to erosion. GPlates allows the user to create a grid of points in deforming regions at which quantities such as time-dependent stretching or thinning factors and crustal thickness can be computed (see workflows in Figure 1). By default, a uniform point spacing of  $0.625^\circ$  is used, but this can be easily



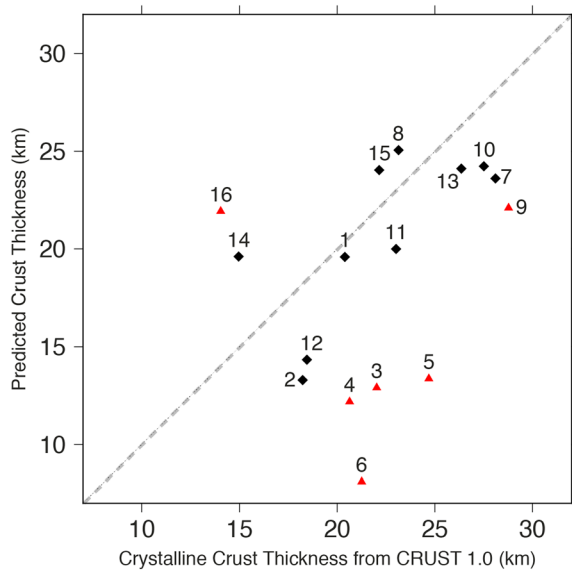


**Figure 10.** Predicted crustal thickness for passive continental margins is compared to the crystalline crustal thickness from CRUST 1.0, with numbers corresponding to regions in Figure 9b. Black triangles represent margins where the predicted crustal thickness differ by 5 km or less on average with CRUST 1.0 crystalline crustal thicknesses, while red diamonds represent a difference greater than 5 km. Dashed line represents a slope of 1.

changed by the user. A complication along rifts and passive margins is that magmatic underplating may thicken the crust, thus making a direct comparison between predicted and observed crustal thickness difficult, unless underplated material can clearly be identified from seismic imaging. In addition, due to the simplicity of our uniform stretching and compression models, our kinematic model is unable to represent effects of strain localization and depth-dependent stretching during rifting. In other words, our model rifts are wide rifts and lack margin-orthogonal strain rate and crustal thickness gradients. As a consequence, we restrict ourselves to comparing our modeled versus observed mean crustal thickness along individual passive margins to crustal thickness from CRUST 1.0 (Pasyanos et al., 2014; Figure 10). We sample CRUST 1.0 along the UCCL of 16 passive margins (Figure 10) at  $0.1^\circ$  (along great circle) intervals and compute the mean UCCL crustal thickness and standard deviation for each passive margin. We choose CRUST 1.0 because it is the most up-to-date global crustal thickness model available to us and allows us to check our model for consistency with a single global crustal thickness model. We note, however, that we used regional, more detailed crustal thickness models to constrain our model in some regions in the North Atlantic and Indian Ocean (see, e.g., Barnett-Moore et al., 2018; Hosseinpour et al., 2013; Williams et al., 2011). The Lord Howe Rise represents a special case, where no original, unthinned crust is preserved. Here the extension model was designed following the assumption that the

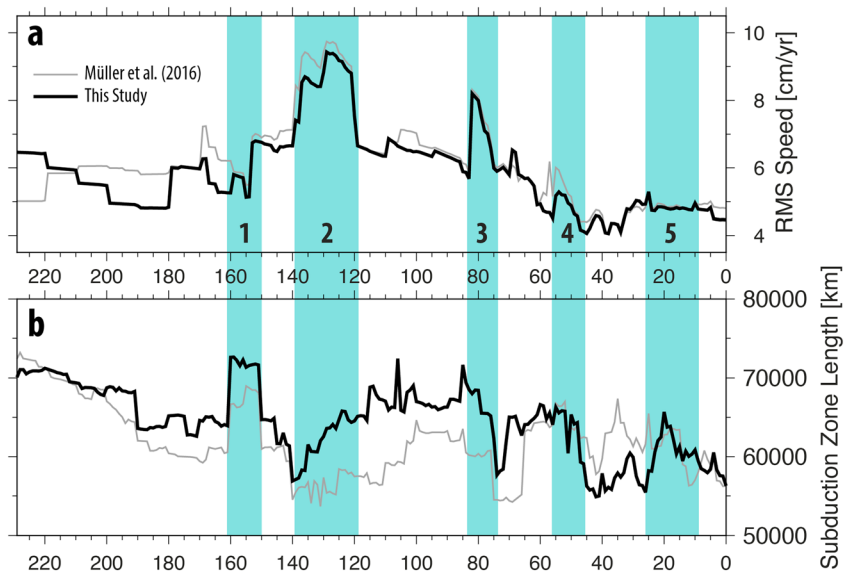


**Figure 11.** (a) Global plate root mean square (RMS) speeds compared between this study (thick black line) and the Müller et al. (2016) model (thin gray line), computed using the method of Zahirovic et al. (2015). Note that the new model is smoother and that some short-lived peaks in RMS speeds have been reduced in magnitude or entirely alleviated (e.g., between 50 and 60 Ma, 100–110 Ma, 120–140 Ma, and 160–170 Ma). (b) Global subduction zone lengths for the model presented in this study (thick black line) compared to the Müller et al. (2016) model (thin gray line). The observed differences primarily reflect changes in modeled subduction history in the eastern and western Tethys (see text). Some significant changes in global subduction zone length, contemporaneous to global plate speed changes, include (1) the onset of subduction in the Arctic, (2) a gradual lengthening of the circum-Pangea girdle of subduction zones following supercontinental breakup, (3) the shutdown of a number of Tethyan subduction zones, (4) changes to subduction zone lengths in the Philippine Sea Plate and New Guinea regions, and (5) changes in subduction zone evolution in the SW Pacific.

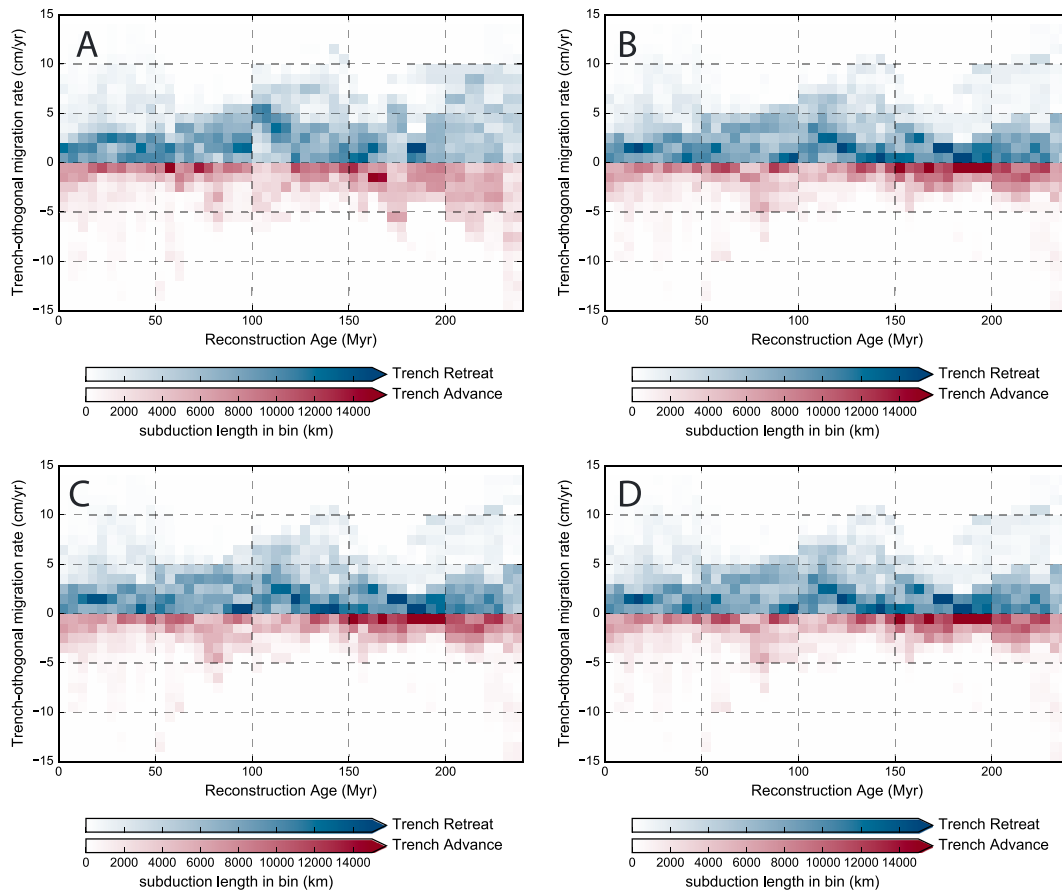


**Figure 12.** Histogram of the trench-orthogonal overriding plate velocity for (a) our unoptimized deforming plate model, using the absolute reference frame from Matthews et al. (2016); and (b) our preferred optimized plate model, using equal weights for fitting hot spot tracks, trench migration, and net rotation optimization for 0–80 Ma and weights of 1 and 0.5 for trench migration and net rotation optimization, respectively, for earlier times. (c) A model with reversed weighting, that is, of 0.5 and 1 for trench migration and net rotation optimization for times before 80 Ma. (d) A model purely based on trench migration (weight 1) and net rotation (weight 0.5) optimization for all model times. Colors are proportional to the length of subduction zones, which is retreating (blue) versus advancing (red) at a given rate. Note the overall improvement in scatter via model optimization, particularly in limiting the majority of trench advance to a relatively narrow band of rates to 0–3 cm/year in all optimized models. Subduction zone retreat still shows somewhat more scatter, but the bulk of retreating trench speeds are confined to 0–4 cm/year in all optimized models.

region was a cordillera-type mountain belt before extension started with an initial thickness of 45 km.

The median difference between modeled and observed crystalline crustal thickness in the 16 passive margins investigated here is 4.0 km. The cases where the crustal thickness is underestimated by our model are volcanic margins, which have likely experienced underplating during their synrift phase, which we cannot take into account. There are six cases where the difference between modeled and observed thickness is negligible (3 km or less in regions 1, 8, 10, 11, 13, and 15 in Figures 9 and 10), two of which (1 and 15) are nonvolcanic margins. In four cases (8, 14, 15, and 16) we have overestimated crustal thickness (Figure 10), reflecting the joint uncertainties in CRUST 1.0 and our crustal stretching model, including the interpreted placement of the UCCL and the boundary between continental and oceanic crust. We also note that there are cases where we overestimate crustal thickness on one margin while underestimating it on the conjugate margin by a similar amount. As an example, this is the case for the Africa–North America conjugate margins and indicates a lateral partitioning of strain across the margins more asymmetric than that implied by our uniform stretching model.

#### 4.3. Optimized Plate-Mantle Absolute Reference Frame

Our optimized model generates absolute plate motions through time that are smoother and undergo less frequent short-term changes in global root mean square speed as compared to the unoptimized model,



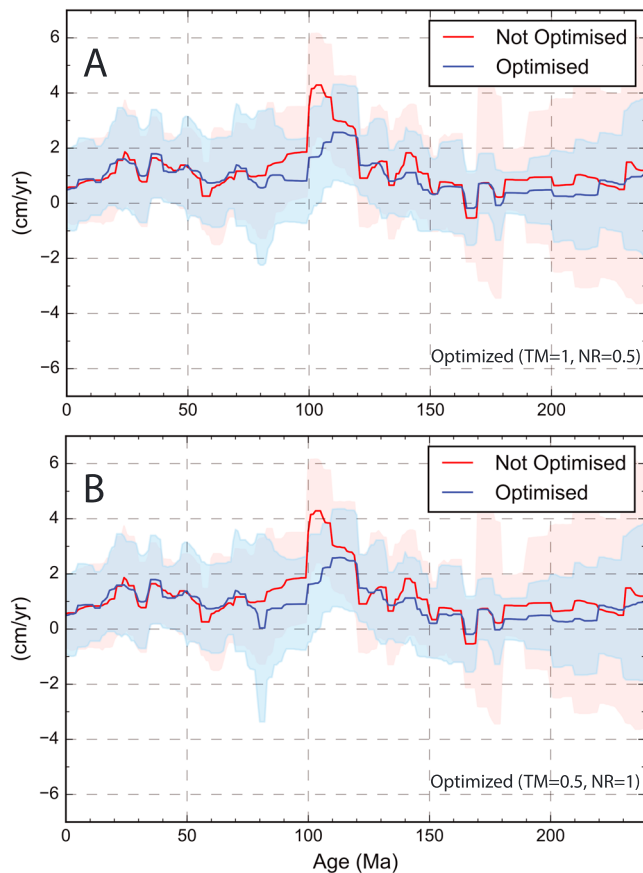


**Figure 13.** (a) Median trench motion with median absolute deviation error envelope for our unoptimized absolute plate motion model in red and our preferred optimized model in blue, and (b) the same comparison but using an optimized model in which the weighting between trench motion (TM) and net rotation (NR) in the optimization is reversed relative to the best fit model. The models are generally quite similar, illustrating that the optimization does not strongly depend on these parameter weights. However, note that around 80 million years the optimized model in Figure 13b produces a peak in median global trench advance that is significantly smaller in our preferred model, even though net rotation is similar in both models (Figure 14), suggesting that our preferred optimization approach is more robust.

using a hybrid hot spot/paleomagnetic reference frame (Figure 11). Some significant changes in plate speeds, contemporaneous with changes in global subduction zone length, relate at least partially to (1) increase in the speed related to Pangea breakup in the central and north Atlantic, (2) northwestward speedup of Africa propagating globally, (3) speedup of the Indian and Izanagi plates, and (4) the acceleration and deceleration of India (Figure 11).

Compared to the unoptimized model, our preferred optimized model exhibits reduced trench migration scatter (Figure 12) and median trench motion (Figure 13), particularly for the Jurassic and Triassic periods, and net rotation is consistently below  $0.2^\circ/\text{Myr}$  (Figure 14). Our preferred model is based on using equal weights for fitting hot spot tracks, trench migration, and net rotation optimization for 0–80 Ma and weights of 1 and 0.5 for trench migration and net rotation optimization, respectively, for earlier times. There is substantial overall improvement in the scatter of trench migration velocities, especially in limiting the bulk of trench advance to a relatively narrow band of rates to 0–3 cm/year (Figures 12a and 12b). Subduction zone retreat exhibits more scatter, particularly between 100 and 150 Ma and before 190 Ma, but the majority of retreating trench speeds are confined to 0–4 cm/year for most of the model.

In order to explore the effect of different parameter choices and weights in our optimization, we show two additional models, one with reversed weighting of trench migration and net rotation optimization for times before 80 Ma, that is, of 0.5 and 1, respectively (Figure 12c), and another model that is purely based on trench migration (weight 1) and net rotation (weight 0.5) optimization for all model times (Figure 12d), without using hot spot tracks. The overarching result of this comparison is that all models provide similar results in terms of trench migration histograms through time (Figures 12b–12d). This implies that hot spot tracks naturally record plate motions in a fairly optimal subduction reference frame. Most hot spots have not moved substantially in a mantle reference frame over the last 80 million years, with only a few exceptions (Dobrovine et al., 2012), and such exceptions are automatically detected in our optimization method. They also record latitudinal and longitudinal plate motions well, unlike paleomagnetic data, and thus provide a reference frame that is compatible with a global distribution of trench migration (Schellart et al., 2008). This also implies that whenever a reference frame is constructed that results in a much broader distribution of trench

motion, including high percentages of fast trench advance or retreat, this is likely an artifact, unless plate tectonics worked in a different way for particular time periods. Such an argument may hold for the early Earth, but likely not for the Phanerozoic. Williams et al. (2015) compared a number of reference frames in this regard, and it is worth noting that moving hot spot reference frames derived from geodynamic models can suffer from the shortcoming of unreasonable trench motion behavior if not constructed in a sensible fashion, certainly for times before 70 Ma.

We note that irrespective of how we assign weights to net rotation and trench migration optimization, we obtain very similar results. This reflects that the two parameters are closely linked. Large net rotation will always result in large spreads in trench migration distributions, and vice versa. However, the connection is nonlinear, as other equivalent relationships, for example, those between finite rotations on a sphere and data constraining plate reconstructions, particularly magnetic anomaly and fracture zone identifications (Chang et al., 1990). Therefore, it is not sufficient to optimize for trench migration or net rotation alone. A comparison of median trench motion and its median absolute deviation (Figure 13), comparing the two optimized models with opposite weighting between trench motion and net rotation, illustrates that the model that favors trench migration minimization (Figure 13a) is free of major artifacts in trench movement

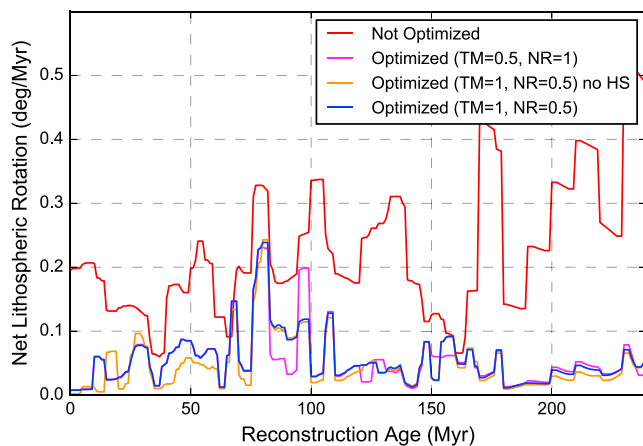


**Figure 14.** Net lithospheric rotation for our unoptimized (red) and preferred optimized (blue) plate model. TM is trench motion optimization, and NR is net rotation optimization, and the values in the inset legend refer to their relative weights. Two other models are shown, one identical to the preferred model optimization but without using hot spot tracks and another with the weights between TM and NR reversed. This time series is computed with a 5-Myr median filter applied to suppress high-frequency noise. Note that all optimized models do not display net rotation higher than  $0.2^\circ/\text{Myr}$  at any time, in compliance with recommendations based on geodynamic models (Becker et al., 2015).

patterns, whereas the model that favors net rotation (Figure 13b) produces a peak in trench advance around 80 Ma. However, both models result in about the same value for net rotation during that time (Figure 14). This suggests that our preferred optimization approach is more robust than the one biased toward net rotation. This is particularly important for the period before 80 Ma, where increasing amounts of synthetic plates provide an independent motivation for relying more on minimizing trench migration than on net rotation, because we generally know much more about the location of subduction zones as compared to our knowledge of now subducted oceanic plates. In conclusion, we assign a smaller weight to net rotation relative to trench migration in our preferred model, particularly because the need to construct synthetic oceanic plates to generate complete global plate models for the geological past contaminates net rotation results in deep time in ways that are difficult to quantify.

## 5. Conclusions

We have constructed the first global plate model that includes plate deformation along major rifts and orogens since rifting of Pangea started in the Early Triassic (240 Ma). The model allows us to quantify how extensional and compressional processes have evolved through space and time during supercontinent fragmentation and dispersal. Distributed plate deformation driven by rifting first peaks in the Late Jurassic (~160–155 Ma) reaching  $30 \times 10^6 \text{ km}^2$ . In the following 50 million years, deformation drops significantly

to a low of  $10 \times 10^6 \text{ km}^2$  in the mid-Cretaceous (~105 Ma), reflecting the transformation of many rifts into passive margins. The total area of plate deformation reaches a high of  $48 \times 10^6 \text{ km}^2$  in the Late Eocene (~35 Ma), driven by the progressive growth of plate collisions as well as the formation of new rift systems in the mid-late Cenozoic. A total of about 35% of the present continental crustal area has been deformed over the last 240 million years, partitioned into  $\sim 50.5 \times 10^6 \text{ km}^2$  that have been extended (~65%) and  $\sim 27 \times 10^6 \text{ km}^2$  that have been compressed (53%). This is a minimum estimate. Along the major passive margins included in this model, the median misfit between modeled crustal thickness and that obtained from the CRUST 1.0 model (Pasyanos et al., 2014) is 4.5 km. This misfit can be reduced in future models by improved assimilation of crustal thickness data into regional rotation models, capturing the synrift phase of passive margins and by accounting for magmatic underplating, where suitable data are available.

We reconstruct absolute plate motions in a mantle reference frame with a joint global inversion using hot spot tracks for the last 80 million years and minimizing global trench migration velocities and net lithospheric rotation. In our optimized model, net rotation is consistently below  $0.2^\circ/\text{Myr}$ , and trench migration scatter is substantially reduced compared to that in unoptimized models. The model results in smoother plate motion paths than conventional mantle reference frames and minimizes major changes in absolute plate motions that are disconnected from concurrent reorganizations of subduction. Therefore, our model is more consistent with the rules of subduction dynamics than are previously published models, considering that absolute plate motions are mainly driven by subduction (Conrad & Lithgow-Bertelloni, 2004).

This community plate model provides a framework for building detailed regional deforming plate networks and for forming a constraint for models of basin evolution and the plate-mantle system. Higher-precision plate models, including deformation and assimilating many more constraints from regional geology than previously possible, will have a range of benefits to different communities, including the study of crustal and lithosphere structure and dynamics, basin analysis, resource exploration, and regional geodynamic models. Our current model still represents a broad simplification of the detailed outlines of the boundaries of stretched or thickened regions, which need to be further refined in the future. The model still lacks many failed rifts and regional orogens. Microcontinents that have been separated from large continents during protracted episodes of rifting are particularly difficult to incorporate in our model and have been excluded. Other challenges include modeling strain rate and crustal thickness gradients across rifts and passive margins and computing surface topography through time considering both lithospheric thinning and postrift

thermal subsidence. Next generation models may also be extended to include deformation of ocean crust. In the future, deforming plate models will provide a basis for creating global paleotopography models, useful for surface process and paleoclimate models. Improvements to regional deforming plate models will benefit from more detailed regional data sets on basin scales being made available by industry and government organizations, including structural and stratigraphic data.

## Acknowledgments

We thank two anonymous reviewers for their detailed, constructive comments, which improved the manuscript substantially. S. Z. and R. D. M. were supported by Alfred P. Sloan grants G-2017-9997 and G-2018-11296 through the Deep Carbon Observatory, and J. C. and R. D. M. were supported by the AuScope National Collaborative Research Infrastructure System (NCRIS) program. M. G. was supported by the National Science Foundation through award EAR-1645775, and E. L. B. was supported by the German Research Foundation (DFG; BR 4900/2-1 grant). The Sydney Informatics Hub provided support for the Artemis high-performance computer used for our plate model optimization. We thank Wenchao Cao, Joanna Tobin, Maxim Adams, and Joe Ibrahim for assistance with plate model editing and figure production. The deforming plate model and associated data can be downloaded at [https://www.earthbyte.org/webdav/ftp/Data\\_Collections/Muller\\_et\\_al\\_2019\\_Tectonics/](https://www.earthbyte.org/webdav/ftp/Data_Collections/Muller_et_al_2019_Tectonics/).

## References

- Alvey, A., Gaina, C., Kuszniir, N., & Torsvik, T. (2008). Integrated crustal thickness mapping and plate reconstructions for the High Arctic. *Earth and Planetary Science Letters*, 274(3–4), 310–321. <https://doi.org/10.1016/j.epsl.2008.07.036>
- Arriagada, C., Roperch, P., Mpodozis, C., & Cobbold, P. (2008). Paleogene building of the Bolivian Orocline: Tectonic restoration of the central Andes in 2-D map view. *Tectonics*, 27, TC6014. <https://doi.org/10.1029/2008TC002269>
- Bai, Y., Wu, S., Liu, Z., Müller, R. D., Williams, S. E., Zahirovic, S., & Dong, D. (2015). Full-fit reconstruction of the South China Sea conjugate margins. *Tectonophysics*, 661, 121–135. <https://doi.org/10.1016/j.tecto.2015.08.028>
- Baldwin, S. L., Fitzgerald, P. G., & Webb, L. E. (2012). Tectonics of the New Guinea region. *Annual Review of Earth and Planetary Sciences*, 40(1), 495–520. <https://doi.org/10.1146/annurev-earth-040809-152540>
- Barnett-Moore, N., Müller, D. R., Williams, S. E., Skogseid, J., & Seton, M. (2018). A reconstruction of the North Atlantic since the earliest Jurassic. *Basin Research*, 30, 160–185. <https://doi.org/10.1111/bre.12214>
- Becker, T. (2006). On the effect of temperature and strain-rate dependent viscosity on global mantle flow, net rotation, and plate-driving forces. *Geophysical Journal International*, 167(2), 943–957. <https://doi.org/10.1111/j.1365-246X.2006.03172.x>
- Becker, T., Schaeffer, A., Lebedev, S., & Conrad, C. (2015). Toward a generalized plate motion reference frame. *Geophysical Research Letters*, 42, 3188–3196. <https://doi.org/10.1002/2015GL063695>
- Boschman, L. M., van Hinsbergen, D. J., Torsvik, T. H., Spakman, W., & Pindell, J. L. (2014). Kinematic reconstruction of the Caribbean region since the Early Jurassic. *Earth-Science Reviews*, 138, 102–136. <https://doi.org/10.1016/j.earscirev.2014.08.007>
- Bower, D. J., Gurnis, M., & Flament, N. (2015). Assimilating lithosphere and slab history in 4-D Earth models. *Physics of the Earth and Planetary Interiors*, 238, 8–22. <https://doi.org/10.1016/j.pepi.2014.10.013>
- Braz, C., Seton, M., Flament, N., & Müller, R. D. (2018). Geodynamic reconstruction of an accreted Cretaceous back-arc basin in the Northern Andes. *Journal of Geodynamics*, 121, 115–132. <https://doi.org/10.1016/j.jog.2018.09.008>
- Brune, S., Williams, S. E., & Müller, R. D. (2017). Potential links between continental rifting, CO<sub>2</sub> degassing and climate change through time. *Nature Geoscience*, 10(12), 941–946. <https://doi.org/10.1038/s41561-017-0003-6>
- Chang, H. K., Kowsmann, R. O., Ferreira Figueiredo, A. M., & Bender, A. A. (1992). Tectonics and stratigraphy of the East Brazil Rift system: An overview. *Tectonophysics*, 213(1–2), 97–138. [https://doi.org/10.1016/0040-1951\(92\)90253-3](https://doi.org/10.1016/0040-1951(92)90253-3)
- Chang, T., Stock, J., & Molnar, P. (1990). The rotation group in plate tectonics and the representation of uncertainties of plate reconstructions. *Geophysical Journal International*, 101(3), 649–661.
- Chorowicz, J. (2005). The East African rift system. *Journal of African Earth Sciences*, 43(1–3), 379–410. <https://doi.org/10.1016/j.jafrearsci.2005.07.019>
- Christeson, G. L., & Barth, G. A. (2015). Aleutian basin oceanic crust. *Earth and Planetary Science Letters*, 426, 167–175. <https://doi.org/10.1016/j.epsl.2015.06.040>
- Conrad, C. P., & Lithgow-Bertelloni, C. (2004). The temporal evolution of plate driving forces: Importance of “slab suction” versus “slab pull” during the Cenozoic. *Journal of Geophysical Research*, 109, B10407. <https://doi.org/10.1029/2004JB002991>
- Døssing, A., Gaina, C., & Brozena, J. M. (2017). Building and breaking a large igneous province: An example from the High Arctic. *Geophysical Research Letters*, 44, 6011–6019. <https://doi.org/10.1002/2016GL072420>
- Dobrovine, P. V., Steinberger, B., & Torsvik, T. H. (2012). Absolute plate motions in a reference frame defined by moving hot spots in the Pacific, Atlantic, and Indian Oceans. *Journal of Geophysical Research*, 117, B09101. <https://doi.org/10.1029/2011JB009072>
- Eagles, G., & Jokat, W. (2014). Tectonic reconstructions for paleobathymetry in Drake Passage. *Tectonophysics*, 611, 28–50. <https://doi.org/10.1016/j.tecto.2013.11.021>
- Embry, A. F., & Dixon, J. (1990). The breakup unconformity of the Amerasia Basin, Arctic Ocean: Evidence from Arctic Canada. *Geological Society of America Bulletin*, 102(11), 1526–1534. [https://doi.org/10.1130/0016-7606\(1990\)102<1526:TBUOTA>2.3.CO;2](https://doi.org/10.1130/0016-7606(1990)102<1526:TBUOTA>2.3.CO;2)
- Flament, N., Gurnis, M., Williams, S., Seton, M., Skogseid, J., Heine, C., & Müller, R. D. (2014). Topographic asymmetry of the South Atlantic from global models of mantle flow and lithospheric stretching. *Earth and Planetary Science Letters*, 387, 107–119. <https://doi.org/10.1016/j.epsl.2013.11.017>
- Gee, J., & Kent, D. (2007). Source of oceanic magnetic anomalies and the geomagnetic polarity timescale. *Treatise Geophysics*, 5, 455–507. <https://doi.org/10.1016/B978-044452748-6/00097-3>
- Genik, G. J. (1992). Regional framework, structural and petroleum aspects of rift basins in Niger, Chad and the Central African Republic (C.A.R.). *Tectonophysics*, 213(1–2), 169–185. [https://doi.org/10.1016/0040-1951\(92\)90257-7](https://doi.org/10.1016/0040-1951(92)90257-7)
- Gibbons, A., Whittaker, J., & Müller, R. (2013). The breakup of East Gondwana: Assimilating constraints from Cretaceous ocean basins around India into a best-fit tectonic model. *Journal of Geophysical Research: Solid Earth*, 118, 808–822. <https://doi.org/10.1002/jgrb.50079>
- Gibbons, A., Zahirovic, S., Müller, R., Whittaker, J., & Yatheesh, V. (2015). A tectonic model reconciling evidence for the collisions between India, Eurasia and intra-oceanic arcs of the central-eastern Tethys. *Gondwana Research*, 28(2), 451–492. <https://doi.org/10.1016/j.gr.2015.01.001>
- Gion, A. M., Williams, S. E., & Müller, R. D. (2017). A reconstruction of the Eureka Orogeny incorporating deformation constraints. *Tectonics*, 36, 304–320. <https://doi.org/10.1002/2015TC004094>
- Goddéris, Y., Donnadieu, Y., Le Hir, G., Lefebvre, V., & Nardin, E. (2014). The role of palaeogeography in the Phanerozoic history of atmospheric CO<sub>2</sub> and climate. *Earth-Science Reviews*, 128, 122–138. <https://doi.org/10.1016/j.earscirev.2013.11.004>
- Gordon, R. G., & Stein, S. (1992). Global tectonics and space geodesy. *Science*, 256(5055), 333–342. <https://doi.org/10.1126/science.256.5055.333>
- Granot, R. (2016). Palaeozoic oceanic crust preserved beneath the eastern Mediterranean. *Nature Geoscience*, 9(9), 701–705. <https://doi.org/10.1038/ngeo2784>

- Grobys, J. W., Gohl, K., & Eagles, G. (2008). Quantitative tectonic reconstructions of Zealandia based on crustal thickness estimates. *Geochemistry, Geophysics, Geosystems*, 9, Q01005. <https://doi.org/10.1029/2007GC001691>
- Gurnis, M., Hall, C., & Lavier, L. (2004). Evolving force balance during incipient subduction. *Geochemistry, Geophysics, Geosystems*, 5, Q07001. <https://doi.org/10.1029/2003GC000681>
- Gurnis, M., Turner, M., Zahirovic, S., DiCaprio, L., Spasojevic, S., Müller, R. D., et al. (2012). Plate tectonic reconstructions with continuously closing plates. *Computers & Geosciences*, 38(1), 35–42. <https://doi.org/10.1016/j.cageo.2011.04.014>
- Gurnis, M., Yang, T., Cannon, J., Turner, M., Williams, S., Flament, N., & Müller, R. D. (2018). Global tectonic reconstructions with continuously deforming and evolving rigid plates. *Computers & Geosciences*, 116, 32–41. <https://doi.org/10.1016/j.cageo.2018.04.007>
- Handy, M. R., Schmid, S., Bousquet, R., Kissling, E., & Bernoulli, D. (2010). Reconciling plate-tectonic reconstructions of Alpine Tethys with the geological–geophysical record of spreading and subduction in the Alps. *Earth-Science Reviews*, 102(3–4), 121–158. <https://doi.org/10.1016/j.earscirev.2010.06.002>
- Handy, M. R., Ustaszewski, K., & Kissling, E. (2015). Reconstructing the Alps–Carpathians–Dinarides as a key to understanding switches in subduction polarity, slab gaps and surface motion. *International Journal of Earth Sciences*, 104(1), 1–26. <https://doi.org/10.1007/s00531-014-1060-3>
- Heine, C., & Brune, S. (2014). Oblique rifting of the Equatorial Atlantic: Why there is no Saharan Atlantic Ocean. *Geology*, 42(3), 211–214. <https://doi.org/10.1130/G35082.1>
- Heine, C., & Müller, R. (2005). Late Jurassic rifting along the Australian North West Shelf: Margin geometry and spreading ridge configuration. *Australian Journal of Earth Sciences*, 52(1), 27–39. <https://doi.org/10.1080/08120090500100077>
- Heine, C., Zoethout, J., & Müller, R. (2013). Kinematics of the South Atlantic rift. arXiv preprint arXiv:1301.2096.
- Hosseinpour, M., Müller, R. D., Williams, S. E., & Whittaker, J. M. (2013). Full-fit reconstruction of the Labrador Sea and Baffin Bay. *Solid Earth Discussions*, 5(2), 917–962. <https://doi.org/10.5194/sed-5-917-2013>
- Hosseinpour, M., Williams, S., Seton, M., Barnett-Moore, N., & Müller, R. D. (2016). Tectonic evolution of Western Tethys from Jurassic to present day: Coupling geological and geophysical data with seismic tomography models. *International Geology Review*, 58(13), 1616–1645. <https://doi.org/10.1080/00206814.2016.1183146>
- Iaffaldano, G., Bodin, T., & Sambridge, M. (2012). Reconstructing plate-motion changes in the presence of finite-rotations noise. *Nature Communications*, 3(1), 1048. <https://doi.org/10.1038/ncomms2051>
- Iaffaldano, G., Hawkins, R., & Sambridge, M. (2014). Bayesian noise-reduction in Arabia/Somalia and Nubia/Arabia finite rotations since ~20 Ma: Implications for Nubia/Somalia relative motion. *Geochemistry, Geophysics, Geosystems*, 15, 845–854. <https://doi.org/10.1002/2013GC005089>
- Kharazizadeh, N., Schellart, W., Duarte, J., & Hall, M. (2016). The variation of crustal stretching and different modes of rifting along the Australian southern continental margin. *Australian Journal of Earth Sciences*, 63(2), 159–174. <https://doi.org/10.1080/08120099.2016.1152998>
- Kirschner, J. P., Kominz, M. A., & Mwakanyamale, K. E. (2010). Quantifying extension of passive margins: Implications for sea level change. *Tectonics*, 29, TC4006. <https://doi.org/10.1029/2009TC002557>
- Kneller, E. A., Johnson, C. A., Karner, G. D., Einhorn, J., & Queffelec, T. A. (2012). Inverse methods for modeling non-rigid plate kinematics: Application to Mesozoic plate reconstructions of the Central Atlantic. *Computers & Geosciences*, 49, 217–230. <https://doi.org/10.1016/j.cageo.2012.06.019>
- König, M., & Jokat, W. (2006). The Mesozoic breakup of the Weddell Sea. *Journal of Geophysical Research*, 111, B12102. <https://doi.org/10.1029/2005JB004035>
- Kreemer, C., Blewitt, G., & Klein, E. C. (2014). A geodetic plate motion and Global Strain Rate Model. *Geochemistry, Geophysics, Geosystems*, 15, 3849–3889. <https://doi.org/10.1002/2014GC005407>
- Kreemer, C., Holt, W. E., & Haines, A. J. (2003). An integrated global model of present-day plate motions and plate boundary deformation. *Geophysical Journal International*, 154(1), 8–34. <https://doi.org/10.1046/j.1365-246X.2003.01917.x>
- Le Breton, E., Handy, M. R., Molli, G., & Ustaszewski, K. (2017). Post-20 Ma motion of the Adriatic Plate: New constraints from surrounding orogens and implications for crust–mantle decoupling. *Tectonics*, 36, 3135–3154. <https://doi.org/10.1002/2016TC004443>
- Lewis, J. L., Day, S. M., Magistrale, H., Castro, R. R., Astiz, L., Rebollar, C., et al. (2001). Crustal thickness of the peninsular ranges and gulf extensional province in the Californias. *Journal of Geophysical Research*, 106(B7), 13,599–13,611. <https://doi.org/10.1029/2001JB000178>
- Liebknecht, U., Appel, E., Ding, L., Neumann, U., Antolin, B., & Xu, Q. (2010). Position of the Lhasa terrane prior to India–Asia collision derived from palaeomagnetic inclinations of 53 Ma old dykes of the Linzhou Basin: Constraints on the age of collision and post-collisional shortening within the Tibetan Plateau. *Geophysical Journal International*, 182(3), 1199–1215. <https://doi.org/10.1111/j.1365-246X.2010.04698.x>
- Liu, S., Gurnis, M., Ma, P., & Zhang, B. (2017). Reconstruction of northeast Asian deformation integrated with western Pacific plate subduction since 200 Ma. *Earth-Science Reviews*, 175, 114–142. <https://doi.org/10.1016/j.earscirev.2017.10.012>
- Macdonald, D., Gomez-Perez, I., Franzese, J., Spalletti, L., Lawver, L., Gahagan, L., et al. (2003). Mesozoic break-up of SW Gondwana: Implications for regional hydrocarbon potential of the southern South Atlantic. *Marine and Petroleum Geology*, 20(3–4), 287–308. [https://doi.org/10.1016/S0264-8172\(03\)00045-X](https://doi.org/10.1016/S0264-8172(03)00045-X)
- Marton, G., & Buffler, R. T. (1994). Jurassic reconstruction of the Gulf of Mexico Basin. *International Geology Review*, 36(6), 545–586. <https://doi.org/10.1080/00206819409465475>
- Matthews, K. J., Maloney, K. T., Zahirovic, S., Williams, S. E., Seton, M., & Mueller, R. D. (2016). Global plate boundary evolution and kinematics since the late Paleozoic. *Global and Planetary Change*, 146, 226–250. <https://doi.org/10.1016/j.gloplacha.2016.10.002>
- Matthews, K. J., Williams, S. E., Whittaker, J. M., Müller, R. D., Seton, M., & Clarke, G. L. (2015). Geologic and kinematic constraints on Late Cretaceous to mid Eocene plate boundaries in the southwest Pacific. *Earth-Science Reviews*, 140, 72–107. <https://doi.org/10.1016/j.earscirev.2014.10.008>
- McKenzie, D. P., & Parker, R. L. (1967). The North Pacific: An example of tectonics on a sphere. *Nature*, 216(5122), 1276–1280. <https://doi.org/10.1038/2161276a0>
- McQuarrie, N., & van Hinsbergen, D. J. (2013). Retrodeforming the Arabia-Eurasia collision zone: Age of collision versus magnitude of continental subduction. *Geology*, 41(3), 315–318. <https://doi.org/10.1130/G33591.1>
- McQuarrie, N., & Wernicke, B. P. (2005). An animated tectonic reconstruction of southwestern North America since 36 Ma. *Geosphere*, 1(3), 147–172. <https://doi.org/10.1130/GES00016.1>
- Morgan, W. J. (1968). Rises, trenches, great faults and crustal blocks. *Journal of Geophysical Research*, 73(6), 1959–1982. <https://doi.org/10.1029/JB073i006p01959>



- Müller, R. D., Cannon, J., Qin, X., Watson, R. J., Gurnis, M., Williams, S., et al. (2018). GPlates—Building a virtual Earth through deep time. *Geochemistry, Geophysics, Geosystems*, 19, 2243–2261. <https://doi.org/10.1029/2018GC007584>
- Müller, R. D., Seton, M., Zahirovic, S., Williams, S. E., Matthews, K. J., Wright, N. M., et al. (2016). Ocean basin evolution and global-scale plate reorganization events since Pangea breakup. *Annual Review of Earth and Planetary Sciences*, 44(1), 107–138. <https://doi.org/10.1146/annurev-earth-060115-012211>
- Nerlich, R., Clark, S. R., & Bunge, H.-P. (2013). The Scotia Sea gateway: No outlet for Pacific mantle. *Tectonophysics*, 604, 41–50. <https://doi.org/10.1016/j.tecto.2012.08.023>
- Pasyanos, M. E., Masters, T. G., Laske, G., & Ma, Z. (2014). LITHO1.0: An updated crust and lithospheric model of the Earth. *Journal of Geophysical Research: Solid Earth*, 119, 2153–2173. <https://doi.org/10.1002/2013JB010626>
- Pease, V., Drachev, S., Stephenson, R., & Zhang, X. (2014). Arctic lithosphere—A review. *Tectonophysics*, 628, 1–25. <https://doi.org/10.1016/j.tecto.2014.05.033>
- Petrov, O., Morozov, A., Shokalsky, S., Kashubin, S., Artemieva, I. M., Sobolev, N., et al. (2016). Crustal structure and tectonic model of the Arctic region. *Earth-Science Reviews*, 154, 29–71. <https://doi.org/10.1016/j.earscirev.2015.11.013>
- Pindell, J. L., & Kennan, L. (2009). Tectonic evolution of the Gulf of Mexico, Caribbean and northern South America in the mantle reference frame: An update. *Geological Society, London, Special Publications*, 328(1), 1–55.
- Reuber, K. R., Pindell, J., & Horn, B. W. (2016). Demerara Rise, offshore Suriname: Magma-rich segment of the Central Atlantic Ocean, and conjugate to the Bahamas hot spot. *Interpretation*, 4(2), T141–T155. <https://doi.org/10.1190/INT-2014-0246.1>
- Rudolph, M. L., & Zhong, S. (2014). History and dynamics of net rotation of the mantle and lithosphere. *Geochemistry, Geophysics, Geosystems*, 15, 3645–3657. <https://doi.org/10.1002/2014GC005457>
- Schellart, W., Stegman, D., & Freeman, J. (2008). Global trench migration velocities and slab migration induced upper mantle volume fluxes: Constraints to find an Earth reference frame based on minimizing viscous dissipation. *Earth-Science Reviews*, 88(1–2), 118–144. <https://doi.org/10.1016/j.earscirev.2008.01.005>
- Scholl, D. W., Buffington, E. C., & Marlow, M. S. (1975). Plate tectonics and the structural evolution of the Aleutian–Bering Sea region. In *GSA Special Papers* (pp. 1–31). America: The Geological Society of America.
- Sciunnach, D., & Garzanti, E. (2012). Subsidence history of the Tethys Himalaya. *Earth-Science Reviews*, 111(1–2), 179–198. <https://doi.org/10.1016/j.earscirev.2011.11.007>
- Segev, A., Rybakov, M., & Mortimer, N. (2012). A crustal model for Zealandia and Fiji. *Geophysical Journal International*, 189(3), 1277–1292. <https://doi.org/10.1111/j.1365-246X.2012.05436.x>
- Şengör, A. C., & Natal'in, B. A. (2001). Riffs of the world. Mantle plumes: Their identification through time. In *Geological Society of America Special Papers* (Vol. 352, pp. 389–482). Boulder, CO: Geological Society of America.
- Shephard, G. E., Müller, R. D., & Seton, M. (2013). The tectonic evolution of the Arctic since Pangea breakup: Integrating constraints from surface geology and geophysics with mantle structure. *Earth-Science Reviews*, 124, 148–183. <https://doi.org/10.1016/j.earscirev.2013.05.012>
- Sigloch, K., & Mihalynuk, M. G. (2017). Mantle and geological evidence for a Late Jurassic–Cretaceous suture spanning North America. *GSA Bulletin*, 129(11–12), 1489–1520.
- Steinberger, B., & Torsvik, T. H. (2008). Absolute plate motions and true polar wander in the absence of hotspot tracks. *Nature*, 452(7187), 620–623. <https://doi.org/10.1038/nature06824>
- Stock, J., & Hodges, K. (1989). Pre-Pliocene extension around the Gulf of California and the transfer of Baja California to the Pacific Plate. *Tectonics*, 8(1), 99–115. <https://doi.org/10.1029/TC008i001p00099>
- Tetley, M. G., Williams, S. E., Gurnis, M., Flament, N., & Müller, R. D. (2019). Constraining absolute plate motions since the Triassic. *Journal of Geophysical Research: Solid Earth*, 124. <https://doi.org/10.1029/2019JB017442>
- Thatcher, W. (2009). How the continents deform: The evidence from tectonic geodesy. *Annual Review of Earth and Planetary Sciences*, 37(1), 237–262. <https://doi.org/10.1146/annurev.earth.031208.100035>
- Torsvik, T., Steinberger, B., Gurnis, M., & Gaina, C. (2010). Plate tectonics and net lithosphere rotation over the past 150 My. *Earth and Planetary Science Letters*, 291(1–4), 106–112. <https://doi.org/10.1016/j.epsl.2009.12.055>
- Torsvik, T., Van der Voo, R., Preeden, U., Mac Niocaill, C., Steinberger, B., Doubrovine, P. V., et al. (2012). Phanerozoic polar wander, palaeogeography and dynamics. *Earth-Science Reviews*, 114(3–4), 325–368. <https://doi.org/10.1016/j.earscirev.2012.06.007>
- Tulloch, A., Ramezani, J., Mortimer, N., Mortensen, J., van den Bogaard, P., & Maas, R. (2009). Cretaceous felsic volcanism in New Zealand and Lord Howe Rise (Zealandia) as a precursor to final Gondwana break-up. *Geological Society, London, Special Publications*, 321(1), 89–118. <https://doi.org/10.1144/SP321.5>
- Van der Voo, R. (1990). The reliability of paleomagnetic data. *Tectonophysics*, 184(1), 1–9.
- van Hinsbergen, D. J., Kapp, P., Dupont-Nivet, G., Lippert, P. C., DeCelles, P. G., & Torsvik, T. H. (2011). Restoration of Cenozoic deformation in Asia and the size of Greater India. *Tectonics*, 30, TC5003. <https://doi.org/10.1029/2011TC002908>
- van Hinsbergen, D. J., Vissers, R. L., & Spakman, W. (2014). Origin and consequences of western Mediterranean subduction, rollback, and slab segmentation. *Tectonics*, 33, 393–419. <https://doi.org/10.1002/2013TC003349>
- Wessel, P., Smith, W., Scharroo, R., Luis, J., & Wobbe, F. (2013). GMT 5: A major new release of the Generic Mapping Tools. *Eos, Transactions of the American Geophysical Union*, 94(45), 409–410. <https://doi.org/10.1002/2013EO450001>
- White, L. T., Gibson, G. M., & Lister, G. S. (2013). A reassessment of paleogeographic reconstructions of eastern Gondwana: Bringing geology back into the equation. *Gondwana Research*, 24(3–4), 984–998. <https://doi.org/10.1016/j.gr.2013.06.009>
- Williams, S. E., Flament, N., Müller, R. D., & Butterworth, N. (2015). Absolute plate motions since 130 Ma constrained by subduction zone kinematics. *Earth and Planetary Science Letters*, 418, 66–77. <https://doi.org/10.1016/j.epsl.2015.02.026>
- Williams, S. E., Whittaker, J. M., Halpin, J. A., & Müller, R. D. (2018). Australian–Antarctic break up and seafloor spreading: Balancing geological and geophysical constraints. *Earth-Science Reviews*, 188, 41–58.
- Williams, S. E., Whittaker, J. M., & Müller, R. D. (2011). Full-fit, palinspastic reconstruction of the conjugate Australian–Antarctic margins. *Tectonics*, 30, TC6012. <https://doi.org/10.1029/2011TC002912>
- Wilson, D. S., & Luyendyk, B. P. (2009). West Antarctic paleotopography estimated at the Eocene–Oligocene climate transition. *Geophysical Research Letters*, 36, L16302. <https://doi.org/10.1029/2009GL039297>
- Wobbe, F., Gohl, K., Chambord, A., & Sutherland, R. (2012). Structure and breakup history of the rifted margin of West Antarctica in relation to Cretaceous separation from Zealandia and Bellingshausen plate motion. *Geochemistry, Geophysics, Geosystems*, 13, Q04W12. <https://doi.org/10.1029/2011GC003742>
- Wood, R., & Stagpoole, V. (2007). Validation of tectonic reconstructions by crustal volume balance: New Zealand through the Cenozoic. *Geological Society of America Bulletin*, 119(7–8), 933–943. <https://doi.org/10.1130/B26018.1>



- Yamano, M., & Uyeda, S. (1985). Possible effects of collisions on plate motions. *Tectonophysics*, 119(1-4), 223–244. [https://doi.org/10.1016/0040-1951\(85\)90040-X](https://doi.org/10.1016/0040-1951(85)90040-X)
- Yang, T., Gurnis, M., & Zhirovic, S. (2016). Mantle-induced subsidence and compression in SE Asia since the early Miocene. *Geophysical Research Letters*, 43, 1901–1909. <https://doi.org/10.1002/2016GL068050>
- Zhirovic, S., Matthews, K. J., Flament, N., Müller, R. D., Hill, K. C., Seton, M., & Gurnis, M. (2016). Tectonic evolution and deep mantle structure of the eastern Tethys since the latest Jurassic. *Earth-Science Reviews*, 162, 293–337. <https://doi.org/10.1016/j.earscirev.2016.09.005>
- Zhirovic, S., Müller, R. D., Seton, M., & Flament, N. (2015). Tectonic speed limits from plate kinematic reconstructions. *Earth and Planetary Science Letters*, 418, 40–52. <https://doi.org/10.1016/j.epsl.2015.02.037>